Structures 91 (2026) 112588

Contents lists available at ScienceDirect

Structures

journal homepage: www.elsevier.com/locate/structures

Concrete-filled aluminium alloy tubular stub columns under eccentric loading

Michaela Gkantou [a,*], Shafayat Bin Ali [b], Nikolaos I. Tziavos [c], Yao Sun [d,e]

[a] School of Engineering and Built Environment, Liverpool John Moores University, UK
[b] Department of Disaster Engineering and Management, Chittagong University of Engineering and Technology, Bangladesh
[c] Department of Civil Engineering, Aston University, Birmingham, UK
[d] College of Civil Engineering, Hunan University, China
[e] State Key Laboratory of Bridge Safety and Resilience, Hunan University, Changsha, China

ARTICLE INFO

Keywords:
Aluminium alloy
Composite structures
Concrete filled
Eccentric loading
Tubular sections
Eurocode 9 (EC9), Eurocode 4 (EC4)

ABSTRACT

The increasing demand for lightweight, durable and corrosion-resistant materials in structural engineering has highlighted the growing potential of aluminium alloys in modern construction. Among these, concrete-filled aluminium tubes (CFATs) are attractive due to their high strength-to-weight ratio and excellent corrosion resistance. This study investigates the structural performance of CFAT stub columns fabricated from 6082-T6 aluminium alloy, which is well suited for structural applications. Despite the advantages of aluminium CFATs, experimental data on their cross-sectional response under combined axial compression and bending remain limited. To address this gap, the present work experimentally investigates CFAT stub columns subjected to eccentric axial loading. A total of eight specimens were tested under nominal eccentricities of 0, 5, 10, and 15 mm. A finite element model was developed and validated against the experimental results, showing excellent agreement in terms of ultimate load capacity, load–displacement response and failure modes. A subsequent numerical parametric study examined the effects of tube thickness and cross-sectional aspect ratio, as well as uniaxial bending about the major and minor axes, to evaluate the influence of geometric parameters on structural performance. Although Eurocode 4 provides design guidance for steel–concrete composite members and Eurocode 9 addresses aluminium structures, specific design provisions for aluminium–concrete composite columns are currently lacking. By drawing on the relevant provisions of both Eurocodes, this study assesses the applicability of interaction curves for moment–compression cross-sectional behaviour using the obtained experimental and numerical results. The findings indicate that the proposed approach provides conservative predictions and offers a preliminary basis for design assessment within the investigated range of parameters.

1. Introduction

Concrete-filled tubes (CFTs) are widely used due to their high strength, durability, and construction efficiency, with composite action between the tube and concrete infill enhancing confinement and delaying buckling [1–3]. Although steel tubes in various cross-sections have been extensively applied [4–10], their self-weight and susceptibility to corrosion can be limiting. Concrete-filled aluminium tubes (CFATs) can address these drawbacks by offering a high strength-to-weight ratio, excellent corrosion resistance, ease of fabrication and handling, and improved aesthetics [11–13]. They are particularly suited to durability-critical and weight-sensitive structural applications, such as marine, coastal, and modular construction environments, where lifecycle performance governs material selection. In such applications, material selection is typically governed by cost, durability, maintenance demands, and constructability considerations, with aluminium being adopted due to its favourable overall performance in these aspects.

Compared to concrete-filled steel tubular (CFST) columns, CFAT members generally exhibit lower stiffness, reduced confinement effectiveness, and greater sensitivity to buckling due to the lower elastic modulus and distinct material behaviour of aluminium. In addition, aluminium sections may be associated with higher material costs and heat-affected zone effects in welded regions. Despite these limitations, CFAT systems benefit from reduced self-weight, high corrosion resistance, and recyclability, making them attractive for specialised

* Corresponding author.
E-mail address: m.gkantou@ljmu.ac.uk (M. Gkantou).

https://doi.org/10.1016/j.istruc.2026.112588
Received 6 October 2025; Received in revised form 16 June 2026; Accepted 5 July 2026
Available online 22 July 2026

Table 1
Summary of measured material properties of aluminium alloys.

Specimen	E (MPa)	$f_{0.1}$ (MPa)	$f_{0.2}$ (MPa)	f_u (MPa)	ε_u (%) (mm/mm)	ε_f (%) (mm/mm)	n
50.8 × 50.8 × 3.3	68,300	257	264	304	7.49	14.70	28.19
50.8 × 50.8 × 4.8	64,500	275	284	318	8.04	8.90	30.92

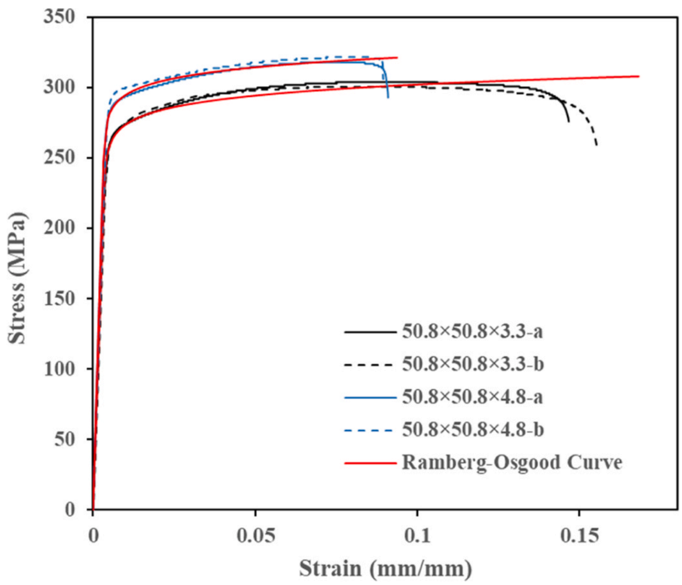

Fig. 1. Stress–strain curves of aluminium alloys.

Table 2
Geometric dimensions of CFAT specimens.

Specimen ID	Depth h (mm)	Width b (mm)	Thickness t (mm)	Length L (mm)	Nominal eccentricity $e_{0,nom}$ (mm)
50.8 × 50.8 × 3.3-e0	50.8	50.8	3.09	153	0
50.8 × 50.8 × 3.3-e5	50.8	50.8	3.09	153	5
50.8 × 50.8 × 3.3-e10	50.8	50.8	3.09	153	10
50.8 × 50.8 × 3.3-e15	50.8	50.8	3.09	153	15
50.8 × 50.8 × 4.8-e0	50.8	50.8	4.76	153	0
50.8 × 50.8 × 4.8-e5	50.8	50.8	4.76	153	5
50.8 × 50.8 × 4.8-e10	50.8	50.8	4.76	153	10
50.8 × 50.8 × 4.8-e15	50.8	50.8	4.76	153	15

applications. For equivalent load capacity, aluminium tubes can reduce column self-weight by up to approximately 17% [14], while the concrete infill enhances the stability of aluminium members [15]. Among structural aluminium alloys, 6082 is increasingly adopted due to its favourable strength and weldability [11].

Despite these advantages, research on CFAT members remains relatively limited compared to CFST systems. Nevertheless, several experimental studies have investigated specific aspects of CFAT structural behaviour. Zhou and Young [16,17] studied the axial compression behaviour of CFAT stub columns, while Feng et al. [18], Chen et al. [19], and Bin et al. [15] investigated the flexural performance of CFAT beams. Studies focusing on column stability and global behaviour have been reported by Georgantzia et al. [20], Rong et al. [21,22], Mi et al. [23], Guo et al. [24], Jiang et al. [25] and Chen et al. [19]. Other investigations have considered the influence of alternative concrete materials, including geopolymer concrete [26] and coral or coral aggregate concrete ([27,28,24,25,29]). However, research addressing eccentric compression behaviour remains comparatively limited and has largely focused on circular hollow sections or slender columns, where global buckling dominates the structural response [21–25]. Consequently, the behaviour of square hollow section (SHS) CFAT stub columns under eccentric compression, where confinement of the concrete core and local buckling of the aluminium tube are critical, remains insufficiently understood.

1.1. Research significance

Recent reviews [30] emphasise the need for further investigation into aluminium–concrete composite members. In this context, experimental evidence on the behaviour of 6082-T6 SHS aluminium alloy stub columns subjected to combined axial load and bending remains scarce. Beyond the limited availability of data, there is also a lack of clear understanding of how aluminium-specific material characteristics influence composite behaviour under eccentric loading. The behaviour of CFAT cross-sections under eccentric compression is governed by the interaction between axial force, bending moment, confinement of the concrete core, and local buckling of the aluminium tube. However, the efficiency and distribution of confinement, as well as the interaction between local buckling and the concrete core, are fundamentally influenced by the lower stiffness and distinct material response of aluminium. These mechanisms may not fully correspond to those observed in steel–concrete composite structures, since aluminium exhibits a lower elastic modulus and a different stress–strain response compared with steel. Consequently, the applicability of CFST design approaches to CFAT members requires further evaluation.

To address these limitations, this study presents an experimental and numerical investigation of 6082-T6 SHS concrete-filled aluminium alloy stub columns subjected to eccentric compression. The research combines experimental testing, validated numerical modelling, and comparative assessment with independent data from the literature to provide a comprehensive evaluation of CFAT behaviour. The study contributes to improved understanding of CFAT structural performance by examining the failure modes, axial load–moment interaction behaviour, and the influence of key parameters, such as eccentricity and section slenderness. The results are used for the assessment of a design framework consistent with Eurocode 4 (EC4) [31] and Eurocode 9 (EC9) [32], highlighting key parameters governing their performance, thereby supporting the development of more reliable design approaches for aluminium–concrete composite structures.

2. Experimental programme

2.1. General

An experimental programme was carried out to investigate the behaviour of CFAT cross-sections under combined compression and bending. Initially, material testing was performed to evaluate the mechanical properties of the concrete and aluminium used. Subsequently, a total of eight stub column specimens were tested under combined compression and bending. Two types of CFAT specimens, comprising 6082-T6 aluminium alloy tubes, were selected to enable direct

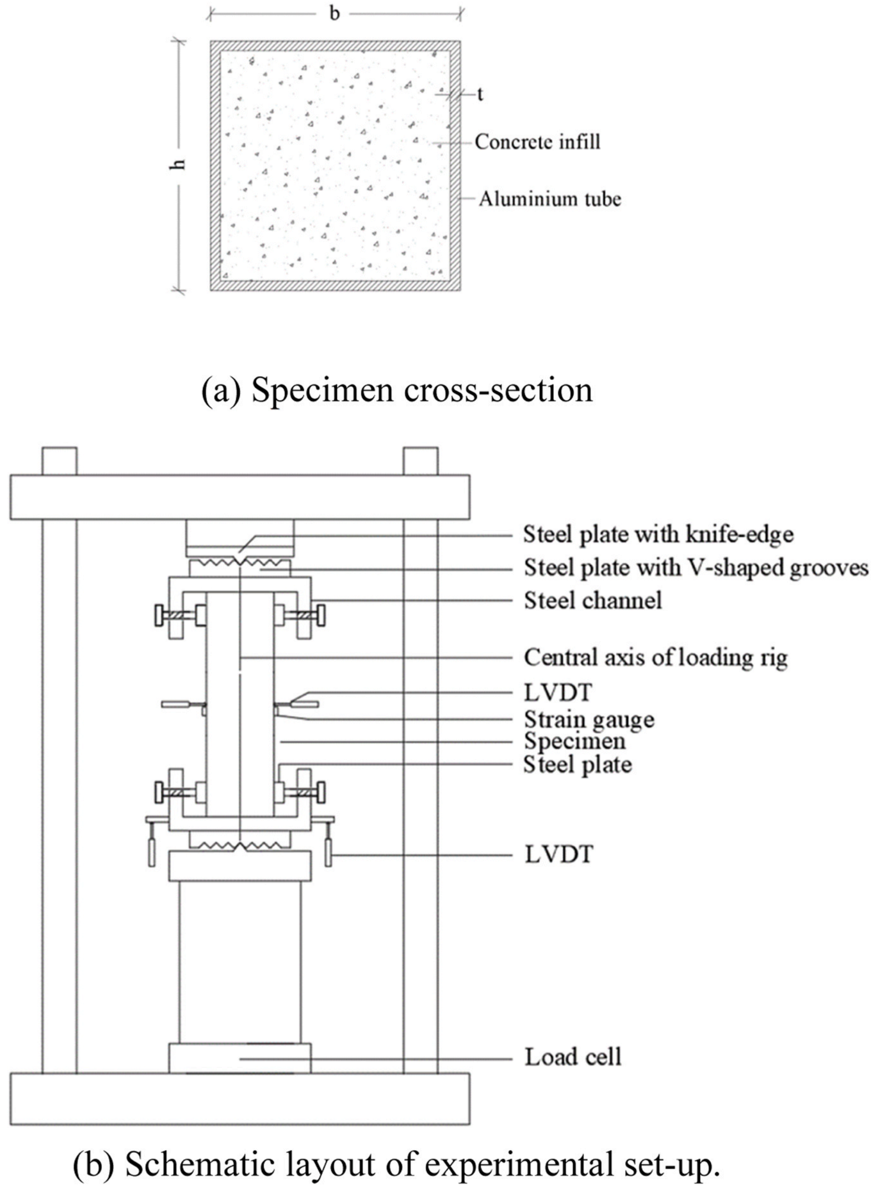

Fig. 2. Experimental set-up.

comparison with previously tested specimens under axial compression [26], global buckling [33] and flexure [15], with the present study extending the investigation to combined axial compression and bending. The aluminium tubes had nominal dimensions of 50.8 × 50.8 × 3.3 mm and 50.8 × 50.8 × 4.8 mm, were infilled with concrete, and were tested under varying levels of applied eccentricity. The concrete was placed in successive layers and consolidated using a vibrating table to ensure appropriate compaction. To prevent leakage during casting, the bottom end of each specimen was sealed with a taped wooden plate. Following casting, all specimens were enclosed in plastic sheeting and left to cure for 28 days, minimising moisture loss throughout the curing process.

2.2. Material testing

The tubular specimens were fabricated using 6082-T6 aluminium alloy. The mechanical properties of the aluminium alloy were determined through tensile coupon tests, extracted from each of the two hollow sections in accordance with the guidelines presented in [34]. Testing was performed under displacement control at a loading rate of 0.2 mm/min and the longitudinal strain was measured using an extensometer.

To capture the observed nonlinear stress–strain behaviour, the material behaviour was modelled using the equations proposed by [35] and later modified by [36]. Table 1 summarises the obtained mechanical properties, where $f_{0.1}$ and $f_{0.2}$ proof stresses represent the yield strengths corresponding to those specific strain offsets, f_u refers to the ultimate tensile strength, ε_u is the strain at ultimate strength, ε_f is the fracture strain and n denotes the Ramberg–Osgood [35] strain hardening exponent. Fig. 1 compares the experimental stress–strain curves obtained from two tensile coupons for each studied thickness, alongside the curves generated using the Ramberg–Osgood model. It is noted that similar values for the examined 6082-T6 material have been reported in other studies [15,20,33,37].

The concrete mixture was designed with a nominal compressive strength of 25 MPa, comprising of ordinary Portland cement, fine and coarse aggregates (up to 10 mm) and water, in a weight ratio of 1:1.5:2.5:0.5. The compressive strength was determined using three concrete cylinders (300 ×150 mm), cast from the same batch as the CFAT specimens and tested and in accordance with [38]. The average compressive strength obtained from these tests was 26.1 MPa. It is noted

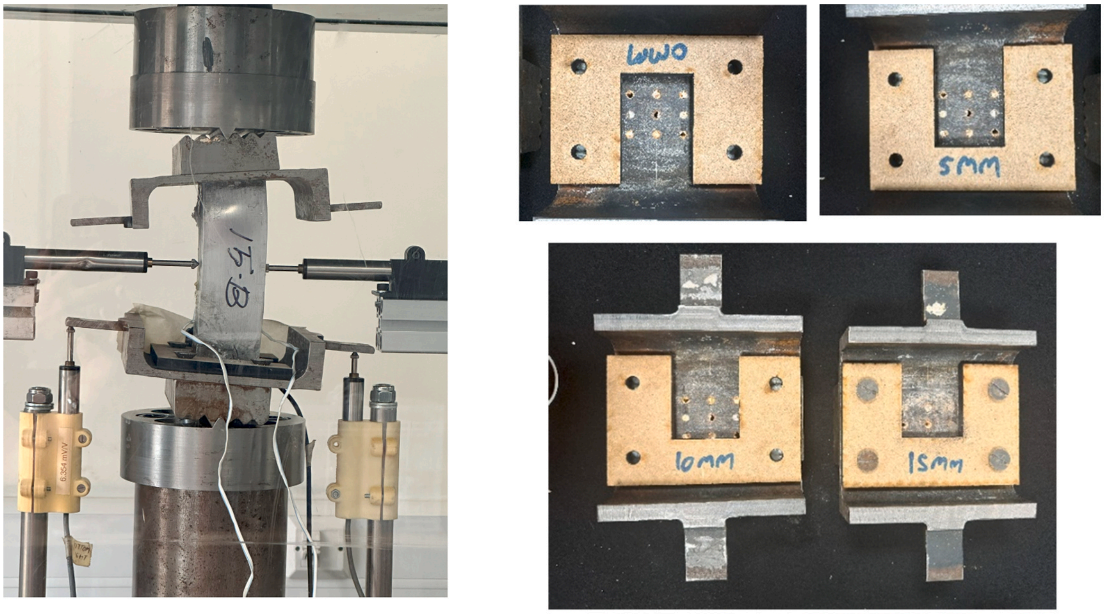

(a) Set-up during testing

(b) Wooden plates employed for intended eccentricity

Fig. 3. Photos of experimental set-up.

Table 3
Key results from eccentric stub column tests.

Specimen ID	Applied actual eccentricity $e_{0,act}$ (mm)	Ultimate load $N_{u,Exp}$ (kN)	Ultimate moment $M_{u,Exp}$ (kNm)	Ultimate mid-height lateral displacement $\delta_{u,Exp}$ (mm)
50.8 × 50.8 × 3.3-e0	0.62	221.74	0.39	1.15
50.8 × 50.8 × 3.3-e5	5.49	177.61	1.43	2.55
50.8 × 50.8 × 3.3-e10	10.03	158.45	2.10	3.23
50.8 × 50.8 × 3.3-e15	15.30	133.56	2.47	3.08
50.8 × 50.8 × 4.8-e0	0.51	355.13	0.71	1.49
50.8 × 50.8 × 4.8-e5	5.55	260.04	2.67	4.70
50.8 × 50.8 × 4.8-e10	10.05	242.91	3.75	5.40
50.8 × 50.8 × 4.8-e15	14.18	202.01	4.15	6.36

that the adopted normal-strength concrete is consistent with published CFAT experimental studies (e.g. [22,19,20,26]) and allows clearer interpretation of cross-sectional interaction under eccentric loading, while avoiding additional variables associated with high-strength concrete. Although higher-strength and advanced concrete materials are increasingly used in modern practice, the present study focuses primarily on the influence of geometric characteristics and loading conditions rather than concrete strength.

2.3. Uniaxial bending and compression testing

Two cross-sectional profiles with varying thicknesses were tested under nominal eccentricities of 0, 5, 10 and 15 mm to investigate their effect on structural behaviour. The geometric details of the specimens are provided in Table 2, and the cross-sectional notations are shown in Fig. 2(a). The specimens had the same external cross-sectional dimensions and concrete grade to those reported in previous studies [15,26], enabling direct comparisons and establishing a benchmark for the ultimate performance of CFAT stub-columns under combined bending and compression. Ultimately, these tests are employed for validation purposes in Section 3.

The applied eccentricities were selected to provide a range of combinations from pure bending to pure compression. Specimen notation in Table 2 follows the cross-sectional dimensions and the corresponding nominal eccentricity ($e_{0,nom}$). The specimen length was set to three times the largest cross-sectional dimension, to ensure the ultimate cross-sectional response is captured while global buckling is avoided.

The combined loading tests were carried out using a 600 kN hydraulic machine, as shown in Fig. 2(b) and Fig. 3(a). Nominal eccentricities were introduced by offsetting each specimen from the centreline using a custom wooden plate, as shown in Fig. 3(b). The top and bottom loading plates interfaced with the loading rig through knife-edge supports, providing pin-ended boundary conditions along the bending axis and fixed-ended conditions along the perpendicular axis. To maintain alignment and prevent lateral movement of the specimens, additional steel channels were loosely bolted with steel plates at both ends. The abovementioned technique has been successfully applied in earlier studies [20].

Instrumentation comprised two linear variable differential transducers (LVDTs), positioned at mid-height for lateral displacement, allowing for the calculation of second order bending moments arising from deviations of the mid-section centroid relative to the load. Two additional LVDTs were symmetrically placed at the lower edge to measure end rotations. Two strain gauges were affixed at mid-height to capture axial strains and determine the actual initial loading eccentricity, as detailed later.

Loading was applied under displacement control with a constant rate of 0.4 mm/min. Throughout testing, the applied load, mid-height and end deflections along with longitudinal strains, were continuously recorded at one second intervals using a data acquisition system.

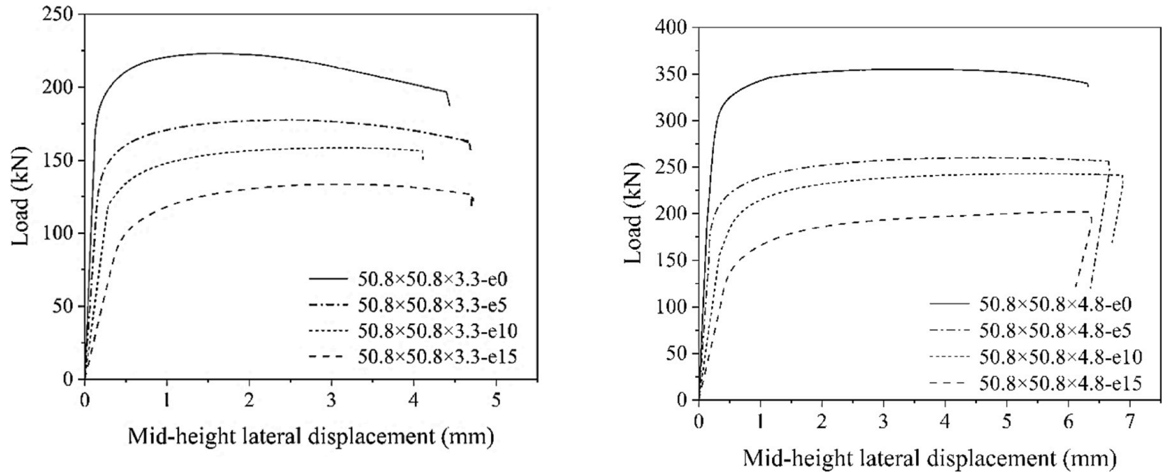

(a) Specimen 50.8×50.8×3.3 (b) Specimen 50.8×50.8×4.7

Fig. 4. Load-mid-height lateral displacement curves.

(i) e0 (ii) e5 (iii) e10 (iv) e15 (i) e0 (ii) e5 (iii) e10 (iv) e15

(a) Specimen 50.8×50.8×3.3 (b) Specimen 50.8×50.8×4.8

Fig. 5. Experimental failure modes.

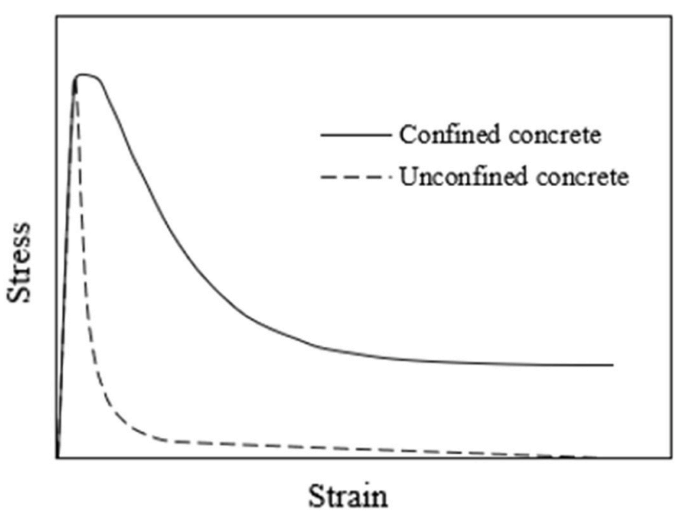

Fig. 6. Compressive response of confined concrete [41].

2.4. Discussion of experimental results

Following the tests, the data from the strain gauges were utilised to determine the exact initial loading eccentricities applied to each specimen. These eccentricities have a significant effect on the response of the specimens under combined compression and bending, therefore accurate values are essential for the development of reliable numerical models from the tests. The nominal eccentricities, i.e. those selected to be applied are tabulated in Table 2, while the actual applied ones are reported in Table 3. The deviation from the nominal value during the experiment is owing to additional, unintentional imperfections and are calculated as follows: For uniaxial bending combined with axial compression, the applied moment M and axial force N read as in Eq. (1)

$$M = N(e_{0,act} + e') \tag{1}$$

Where $e_{0,act}$ is the actual initial eccentricity and e' represents the additional eccentricity induced by second-order effects. The summation of these terms represents the total eccentricity at the specimen's mid-height. In the elastic loading phase, the actual initial eccentricity ($e_{0,act}$) can be derived from the recorded axial strains on the concave ($\varepsilon_{concave}$) and convex (ε_{convex}) faces of the specimens, using the theoretical relationship between the applied bending moment, axial load and strain as follows:

$$e_{0,act} = \frac{2I(1+\psi)}{Ah(1-\psi)} - e' \tag{2}$$

Where, A and I are the cross-sectional area and the second moment of area of the composite section, and ψ is the ratio of measured strains between the concave and convex faces ($\varepsilon_{concave}/\varepsilon_{convex}$) as described in [39]. The key experimental results, including the calculated actual eccentricity ($e_{0,act}$), the maximum applied load and bending moment, as well as the corresponding average lateral displacement at mid-height, are presented in Table 3.

The load–mid-height average lateral displacement curves are presented in Fig. 4, showing the structural response of the CFAT specimens under varying levels of loading eccentricity. For the thinner-walled

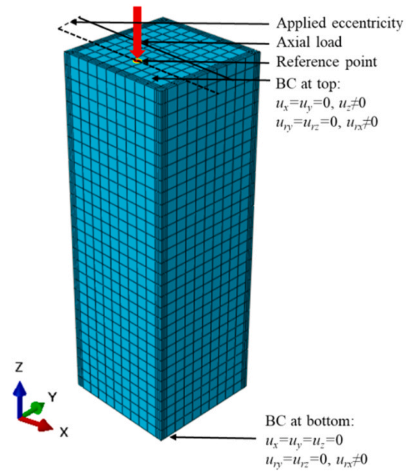

(a) FE model of CFAT stub column

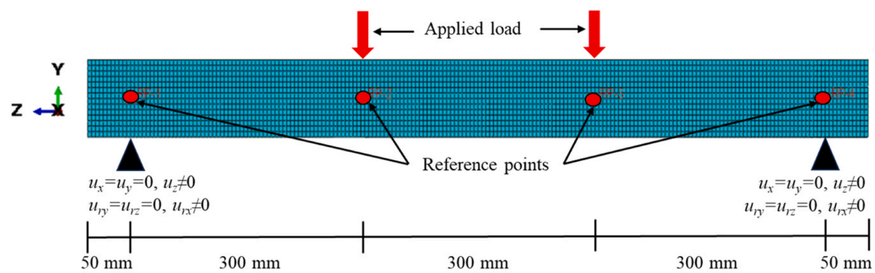

(b) FE model of CFAT beam [15]

Fig. 7. Loading and boundary conditions of FE models.

section (50.8 ×50.8 ×3.3), the concentrically loaded specimen (e0) exhibits the highest ultimate load, exceeding 220 kN. The response is initially linear, followed by gradual stiffness degradation prior to peak load, indicating progressive yielding of the aluminium tube. With increasing eccentricity (e5, e10, e15), a progressive reduction in ultimate load was observed. A clear reduction in initial stiffness is also evident, reflecting increased bending contribution and stress redistribution across the section. At e15, the load capacity drops significantly to around 130 kN accompanied by larger lateral displacements, highlighting the growing influence of second-order effects. A similar eccentricity-driven reduction in strength and stiffness has been reported in previous CFAT studies on circular cross-section subjected to eccentric compression [28], where increasing load eccentricity progressively shifts the response from confinement-dominated compression to bending-controlled sectional behaviour. This is also in line with findings of [23] who concluded that increasing eccentricity reduces the hoop confinement effect provided by the aluminium tube to the internal concrete.

The thicker-walled cross-sections (50.8 ×50.8 ×4.8 mm) exhibit higher load-bearing capacity for all tested eccentricities, with the concentric capacity over 350 kN, following similar trends of decreasing stiffness and reduced peak load with increasing eccentricity. The increased aluminium thickness enhances axial stiffness and local buckling resistance, thereby improving confinement to the concrete core and delaying instability. Collectively, the tested specimens provide sufficient evidence of stable composite interaction under combined loading. The thicker sections also show reduced sensitivity to eccentricity, while thinner sections exhibit a greater reduction in axial capacity as eccentricity increases. This confirms that tube stiffness plays a key role in maintaining sectional integrity under combined bending and compression. This observation is consistent with earlier experimental and numerical investigations on CFAT members (e.g [18,20]) which demonstrated that tube thickness and section slenderness are dominant parameters governing confinement efficiency and ultimate capacity.

Fig. 5 shows the deformed specimens after failure. In both groups, noticeable plastic deformation is observed. There is no prominent surface spalling, whilst local buckling deformations were observed near the ends of the specimens subjected to concentrically applied loads. Similar failure modes [26,28] have been previously documented in CFAT stub columns [26], where the relatively low elastic modulus of aluminium limits confinement compared to CFST systems.

3. Numerical Programme

To further study thebehaviour of CFAT stub columns under eccentric compressive loading, a three-dimensional finite element (FE) model was developed using ABAQUS software [40]. The developed model was validated against the experimental data of Section 2 and data from literature. Using this validated model, a numerical parametric study was carried out to investigate the effect of variation of different design parameters. To establish the full interaction performance of the CFAT cross-section, including both extremes -pure compression and pure bending- a numerical model of CFAT beams was also developed and validated against experimental results from the literature, ensuring accurate representation of the pure bending behaviour.

3.1. Modelling assumptions

The geometric dimensions and material properties of all CFAT stub columns, as reported in Table 1 and Table 3 were used to develop the FE models. The aluminium hollow tube and inner concrete core were modelled using eight-node hexahedral solid elements (C3D8R). Based

Table 4
Ratios of FE over test ultimate load of CFAT stub columns and CFAT Beams.

Reference	Specimen	Cross-section	Aluminium grade	Concrete grade	$N_{u,FE}/N_{u,Exp}$ (stub columns) or $M_{u,FE}/M_{u,Exp}$ (beams)
this study (stub columns)	50.8 × 50.8 × 3.3-e0	SHS	6082-T6	C20	0.99
	50.8 × 50.8 × 3.3-e5	SHS	6082-T6	C20	1.02
	50.8 × 50.8 × 3.3-e10	SHS	6082-T6	C20	0.99
	50.8 × 50.8 × 3.3-e15	SHS	6082-T6	C20	1.02
	50.8 × 50.8 × 4.8-e0	SHS	6082-T6	C20	0.94
	50.8 × 50.8 × 4.8-e5	SHS	6082-T6	C20	1.06
	50.8 × 50.8 × 4.8-e10	SHS	6082-T6	C20	0.98
	50.8 × 50.8 × 4.8-e15	SHS	6082-T6	C20	1.05
[29] (stub columns)	CC−20–2	SHS	6061-T6	C20	1.04
	CC−30–2	SHS	6061-T6	C30	0.99
	CC−40–2	SHS	6061-T6	C40	1.03
	CC−20–4	SHS	6061-T6	C20	1.05
	CC−30–4	SHS	6061-T6	C30	0.99
	CC−40–4	SHS	6061-T6	C40	1.01
	CC−20–6	SHS	6061-T6	C20	0.99
	CC−30–6	SHS	6061-T6	C30	1.00
	CC−40–6	SHS	6061-T6	C40	1.04
[15] (beams)	76.2 × 76.2 × 1.6-C	SHS	6082-T6	C20	0.96
	76.2 × 76.2 × 3.3-C	SHS	6082-T6	C20	1.02
	76.2 × 76.2 × 4.8-C	SHS	6082-T6	C20	0.94
	76.2 × 76.2 × 6.4-C	SHS	6082-T6	C20	0.94
	76.2 × 25.4 × 3.3-C	RHS	6082-T6	C20	0.98
	76.2 × 38.1 × 3.3-C	RHS	6082-T6	C20	0.92
	76.2 × 50.8 × 3.3-C	RHS	6082-T6	C20	0.92
	101.6 × 25.4 × 3.3-C	RHS	6082-T6	C20	0.94
	101.6 × 50.8 × 3.3-C	RHS	6082-T6	C20	0.94
	101.6 × 76.2 × 3.3-C	RHS	6082-T6	C20	0.94
	Mean				**0.99**
	Coefficient of Variation (COV)				**0.04**

on a mesh sensitivity study, a mesh size of 5 mm was selected and generated using the structured meshing technique for the aluminium tube and concrete core. A minimum of three elements through thickness were employed for each tube. Similar mesh sizes have been shown to provide good accuracy, while enabling efficient simulations in comparable structures [20]. The material behaviour of the aluminium section was simulated using the elastic-plastic model of ABAQUS. The elastic behaviour of the aluminium section was modelled using the modulus of elasticity reported in Table 1 and a Poisson's ratio of 0.33. Material yielding was determined using the von Mises criterion, while isotropic hardening was employed. The stress-strain coupon test data were used as input in ABAQUS, by converting them to true stress-logarithmic plastic strain data.

Concrete was modelled using the concrete damage plasticity (CDP) model. This model has been used successfully in earlier studies of concrete filled aluminium composite structures [15,20,33,37]. For the elastic response of concrete, the modulus of elasticity value was 29.33 GPa and was determined according to Eurocode 2 [31], while the Poisson's ratio value was taken as 0.2. The dilation angle that controls volumetric expansion (dilatancy) of concrete when it undergoes plastic shear deformation, was taken equal to 40° in line with earlier numerical studies [41], whereas the viscosity parameter and flow potential eccentricity (ε) were set equal to 0 and 0.1 respectively. The ratio between biaxial and uniaxial compressive strength $(\frac{fb_0}{fc_0})$ was set to 1.17 based on the equation suggested by Papanikolaou and Kappos [42] and the value of compressive meridian (K_c) was calculated as 0.72 according to the equation suggested by and Yu et al. [43]. The tension softening behaviour of concrete (post-peak cracking) was defined using a stress–crack opening displacement relationship, based on the fracture energy concept [40], which represents the energy required to open a unit area of a crack.

The confinement effect in concrete modelling is considered by adopting the confined concrete models proposed by [41] shown in Fig. 6. The model has been initially developed for steel-concrete structures but has been successfully applied in earlier studies [15,20,33,37] focusing on aluminium-concrete structures. According to [30], the behaviour of the concrete until the ultimate strength is reached is considered the same as the unconfined concrete as the interaction between the two materials will be initiated at the later stages due to variation of the Poisson's ratio. Subsequently, the strength increases due to the confinement effect, which is represented by a horizontal plateau followed by a descending branch with high ductility. Consistent with the aforementioned studies ([15,20,33,37]), confinement in the present finite element framework is not imposed through a predefined enhancement coefficient. Instead, it develops progressively through equilibrium and compatibility between the aluminium tube and the concrete core. As axial loading increases and concrete dilation occurs, interaction stresses evolve naturally via contact interaction and nonlinear material behaviour, allowing passive confinement and stiffness degradation to be captured at the structural level. The tensile strength of the confined concrete is considered to be 10% of the compressive strength [41] and a descending portion is added after the tensile strength, considering the fracture energy [44,45,46].

The surface-to-surface contact model in ABAQUS was applied to simulate the interaction of the outer section and the concrete core. In this model, the concrete surface was considered as the master surface, and the inner surface of the hollow tube was assigned as the slave surface. In the vertical direction, a hard contact relationship between two surfaces was used to ensure zero penetration under compression and to allow separation subjected to tension. In the horizontal direction, the Coulomb friction model with a 0.3 coefficient was applied to consider sliding between the surfaces, in line with similar past studies [47].

To replicate the test boundary conditions, reference points (RP) were created at the centroid of both ends of the specimen to apply a concentric compressive load using the displacement control method. For eccentric compression, both RP were moved to the desired loading position. It is considered that the top RP can move along the loading

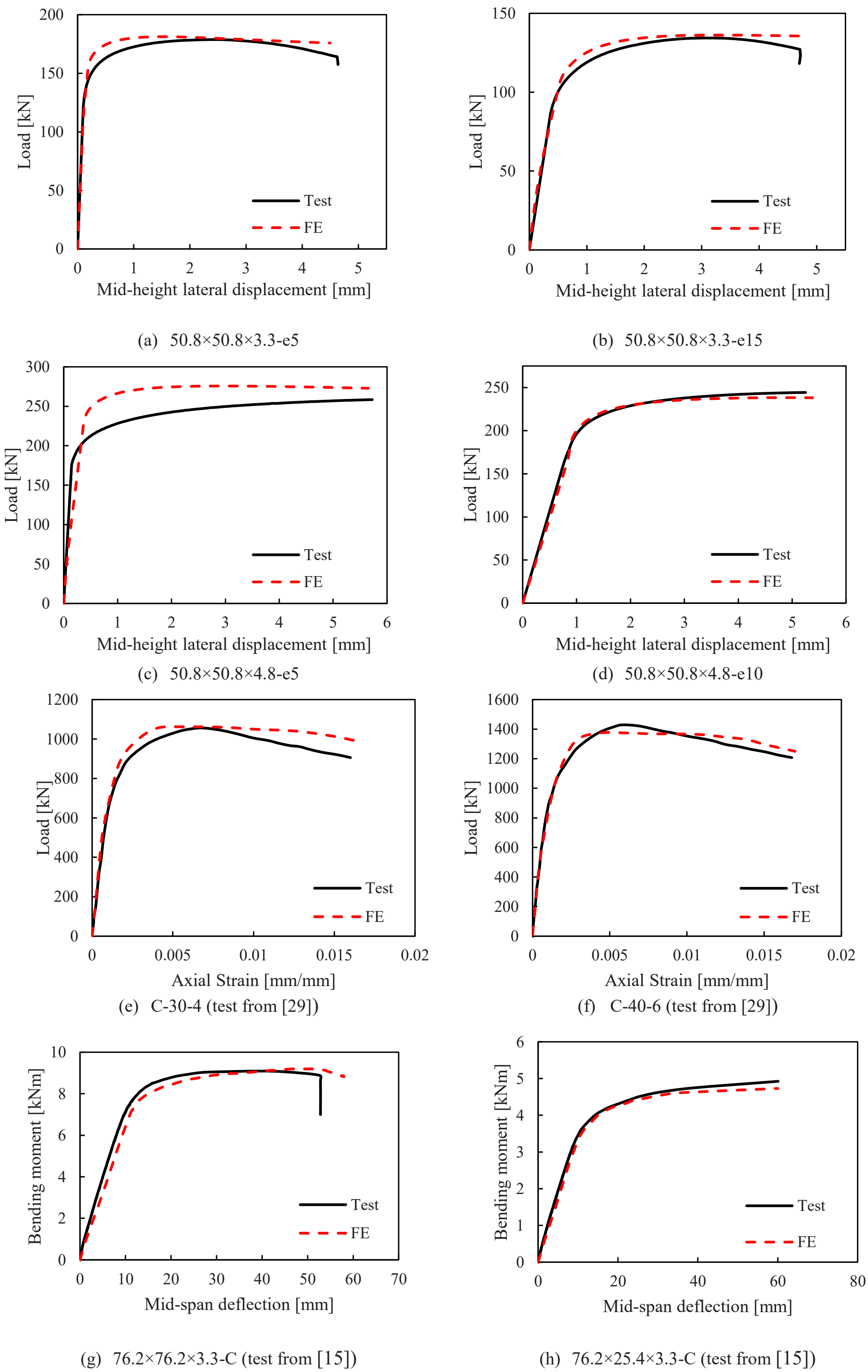

Fig. 8. Comparison between test and FE responses for CFAT columns and beams.

direction, i.e., Z direction and both RP have rotational degree of freedom around the X direction. Fig. 7 displays the loading and boundary conditions of the developed FE model of CFAT stub columns and CFAT beam developed and validated by [15]. The residual stresses were not considered in the FE model, as their presence is typically very low in aluminium sections due to the production process as reported in [20]. The effect of local geometric imperfections has been found to be negligible in similar structures [47], due to the confinement provided to the

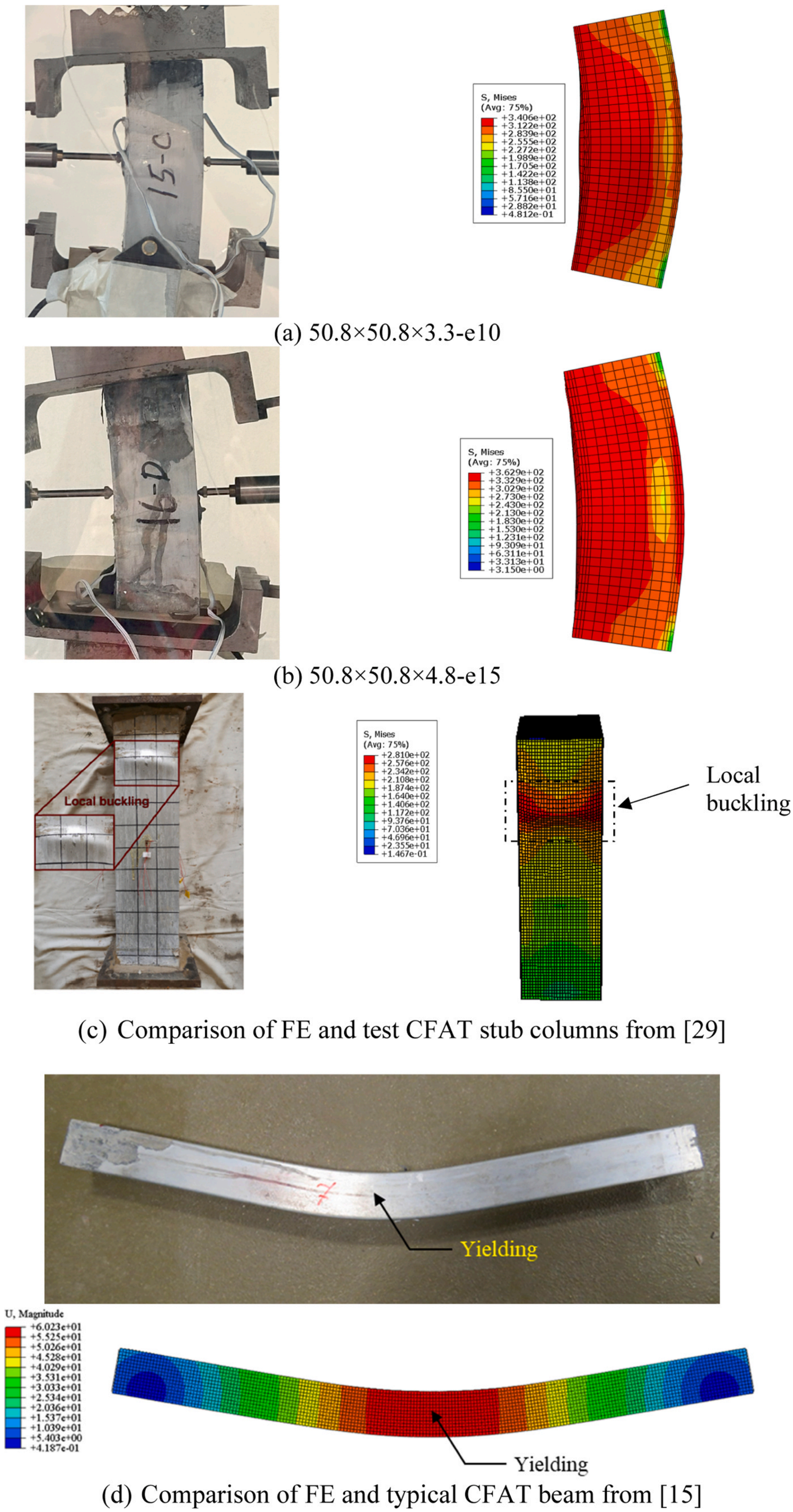

Fig. 9. Comparison between experimental and numerical failure modes.

Table 5
List of key parameters included in the parametric study.

	Total analyses: 160
4 cross-sectional thickness of aluminium tube (mm)	• 1.6 • 3.3 • 4.8 • 6.4
3 aspect ratios (h×b)	• 50.8 × 50.8 (h/b=1) • 76.2 × 50.8 (h/b=1.5) • 101.6 × 50.8 (h/b=2)
Bending axis	• major • minor
8 loading cases	ψ= + 1 (e=0 mm; axial compression) ψ= + 0.65 ψ= + 0.50 ψ= + 0.35 ψ= 0 ψ= −0.35 ψ= −0.65 ψ= −1 (pure bending)

metal tube by the concrete and hence have not been considered herein.

It should be noted that the selected CDP parameters, friction coefficient, and the omission of residual stresses and initial imperfections were adopted based on previous studies and validated against the present test results (see Section 3.2). A systematic sensitivity study of these modelling assumptions was beyond the scope of the present work and may be considered in future research.

3.2. Validation of FE models

For validation purposes, the FE failure pattern, the axial compressive load vs mid-height lateral displacement response and the maximum compressive load of each CFAT FE model were compared with those obtained from the test. In Table 4, the ratio of the FE and test ultimate strength of all stub columns is listed. Good agreement is observed between the test and FE results, with a mean and coefficient of variation (COV) of 1.01 and 0.04, respectively. Fig. 8(a-d) shows the comparison of the test and FE load vs mid-height lateral displacement curves. Failure patterns are compared in Fig. 9(a-b) where it can be observed that the developed FE model closely replicates the failure pattern of CFAT specimens.

In addition to the eight specimens tested herein, nine specimens from study [29] were included in the validation. In that study, axial compression tests were conducted on nine coral concrete-filled aluminium square stub columns to characterise their failure modes, load-carrying capacity, and load–deformation behaviour, while also examining the influence of concrete strength. The corresponding strength ratios and load-deformation comparisons are presented in Table 4 and Fig. 8(e–f), with failure pattern replication shown in Fig. 9 (c). It is noted that the validation against test data of [29] involved also

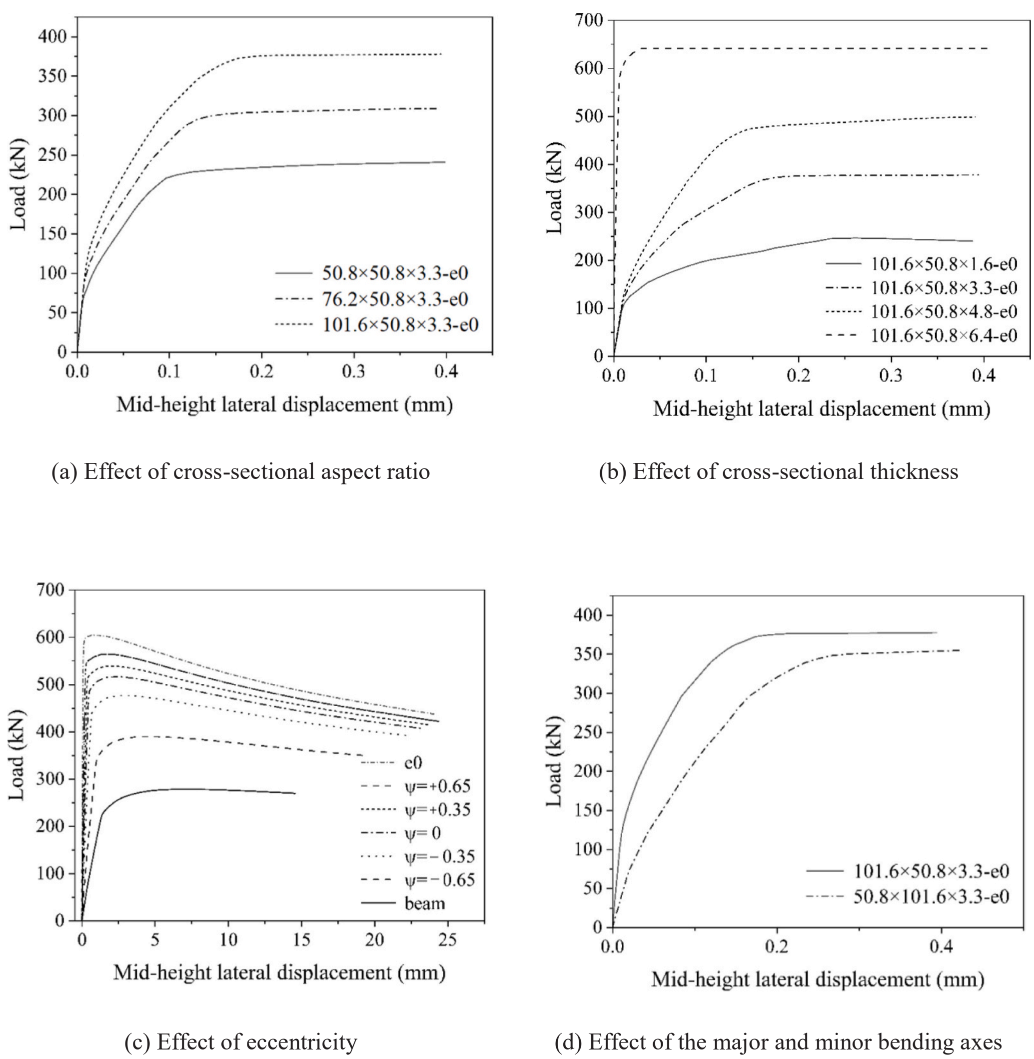

(a) Effect of cross-sectional aspect ratio (b) Effect of cross-sectional thickness

(c) Effect of eccentricity (d) Effect of the major and minor bending axes

Fig. 10. Results from parametric studies.

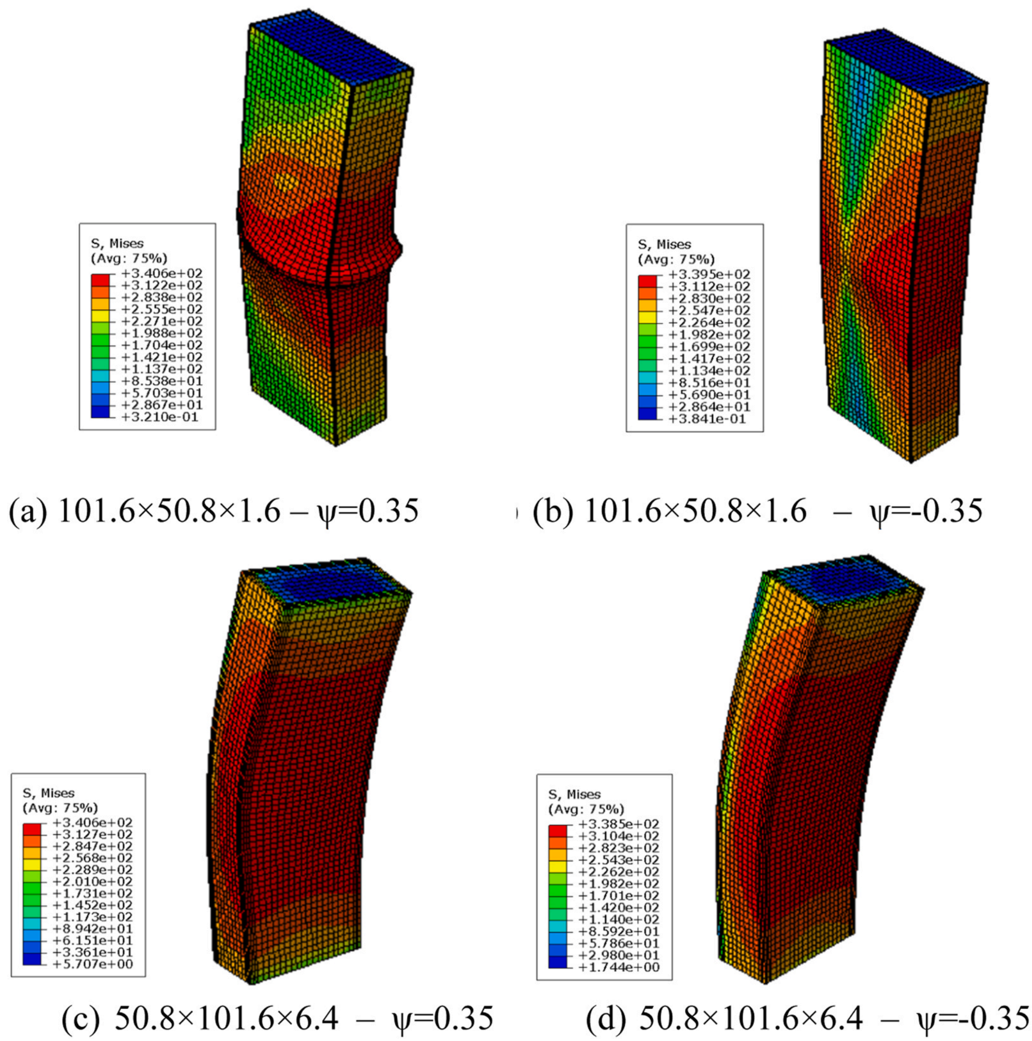

Fig. 11. Failure modes obtained from parametric studies.

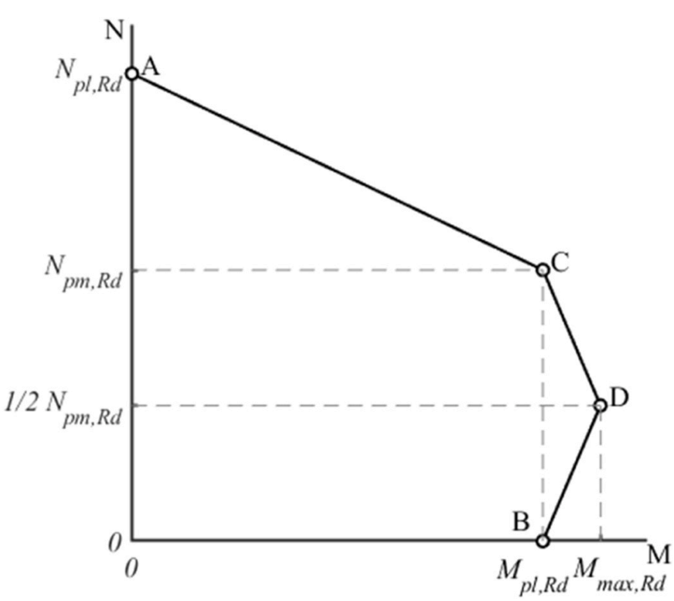

Fig. 12. Simplified M-N interaction curve according to [31].

higher-strength concrete (e.g., C40), demonstrating the model's applicability beyond the concrete strength range adopted in this study.

In addition, a CFAT beam numerical model was also developed and validated against the test data by [15] in order to generate the interaction diagram of CFAT cross-sections, including the pure bending scenario. The study in [15] presented experimental and numerical investigations on 10 square and rectangular 6082-T6 aluminium tubular beams to evaluate their in-plane bending behaviour, including failure modes, flexural strength, stiffness, ductility and moment–deflection response. Fig. 8(g)-(h), Fig. 9d and Table 4, show the accuracy of FE model of CFAT beam, in terms of moment vs mid-span deflection curves, failure modes and ultimate moments, respectively, compared to those reported in [15].

Overall, the comparison across all 27 tests shows very good agreement between numerical and experimental results, including good representation of failure modes and load–deformation response, confirming the robustness and reliability of the adopted modelling framework.

3.3. Parametric study

Using the validated FE model of CFAT stub column and CFAT beam [15], an extensive parametric study was conducted to generate more structural performance data of CFAT cross-section under combined uniaxial bending and compression. An average test stress–strain

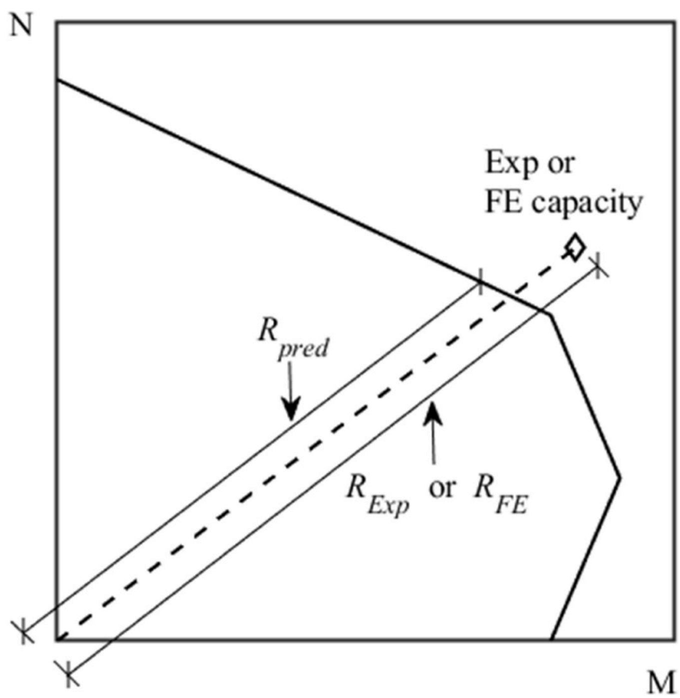

Fig. 13. Definition of ratio of experimental or numerical ultimate capacity to design prediction $R_{Exp,FE}/R_{pred}$.

relationship with $f_{0.2}$= 271.2 MPa was applied to consider the material properties of aluminium hollow sections. A total of 160 FE models, including 140 stub columns and 20 beams, were developed. The list of key parameters included in the parametric study are detailed in Table 5. The parametric analysis was designed to generate additional data points along the M–N interaction curve. As the experimental study was limited to square cross-sections, the numerical investigation was extended to rectangular sections with aspect ratios greater than one, considering bending about both major and minor axes. Finally, while only two width-to-thickness ratios were considered in the experimental tests, four different ratios were examined in the FE analysis in order to extend the investigated range. In particular, three cross-sectional dimensions were considered for both column and beam specimens: 50.8 × 50.8 mm, 76.2 × 50.8 mm, and 101.6 × 50.8 mm. These configurations correspond to three aspect ratios, addressing cases of both major-axis and minor-axis bending combined with axial compression. For each aspect ratio, four thicknesses – ranging from 1.6 mm to 6.4 mm – were examined to assess the influence of local slenderness. A total of seven loading scenarios were studied, defined by varying the ψ ratio, covering a full spectrum from pure compression to pure bending conditions. The concrete strength was set equal to 25 MPa, similarly to the experimental campaign. Previous CFAT studies that examined the influence of concrete grade (e.g., He et al. [28,27]; Wang et al. [48], Jiang et al. [25]) have shown that increasing concrete strength enhances axial capacity and stiffness but does not fundamentally alter the governing failure modes. As its effect is secondary to parameters such as eccentricity and tube thickness, concrete grade is treated as a contributing rather than governing variable in this cross-sectional study. The parametric investigation primarily aimed to expand the dataset in terms of thickness, cross-sectional geometry and bending axis.

Typical load–mid-height lateral displacement curves are presented in Fig. 10. Fig. 10(a) shows the influence of cross-sectional size on the structural performance of CFAT stub columns, presenting load–displacement curves for specimens with varying aspect ratios, while maintaining a constant applied eccentricity and thickness of the aluminium tube. The results indicate that both the initial stiffness and ultimate load capacity increase with larger cross-sectional dimensions, as the increased concrete volume and larger confinement area contribute to enhanced resistance against compressive loads. Fig. 10(b) presents the influence of the thickness of the aluminium on the structural performance, with the applied eccentricity and aspect ratio kept constant. The results demonstrate that increasing the aluminium tube thickness significantly enhances the ultimate load capacity of the stub column. Fig. 10(c) displays the FE results for a selected specimen, with constant aspect ratio and thickness, subjected to varying levels of eccentricity. An anticipated trend is noticed where the ultimate load is decreased with the increase of loading eccentricity. Fig. 10(d) shows the effect of the bending axis by comparing the responses of major and minor axis bending, showing that bending about the minor axis results in lower ultimate strength and stiffness.

Fig. 11 shows typical failure modes of the parametric study and particularly, the numerical failure modes of rectangular aluminium hollow sections under different bending conditions and thicknesses. Figures (a)-(b), representing the thinner sections under major-axis bending and compression, exhibit clear local buckling within the compression region, including for the moment gradient case of ψ = −0.35, indicating reduced resistance to local instability and higher local stress concentrations. In contrast, Figures (c)-(d), corresponding to the thicker 6.4 mm aluminium sections under minor-axis bending and compression, show predominantly global flexural deformation with no noticeable local buckling. The thicker sections maintain better sectional stability and exhibit a flexural-dominated response.

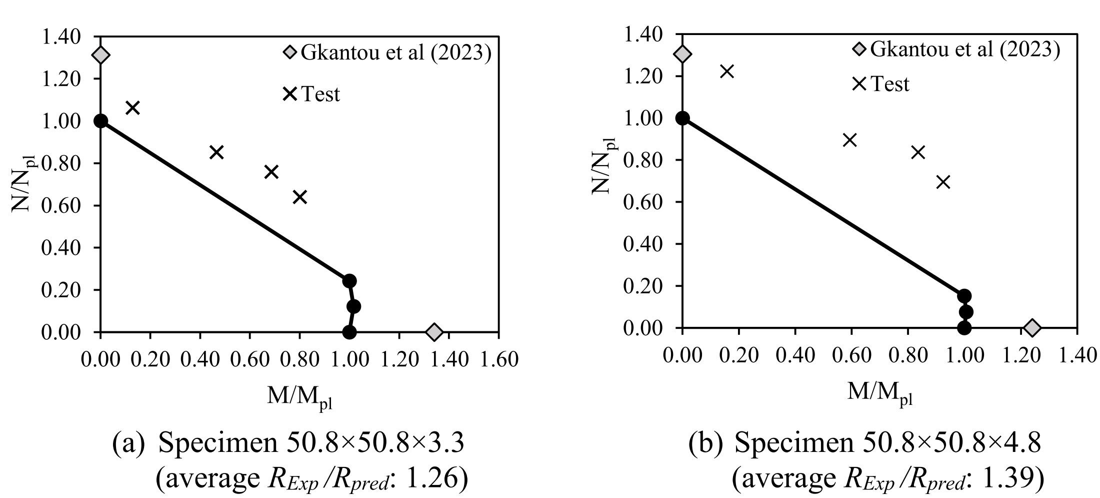

Fig. 14. Eurocode assessment based on experimental data.

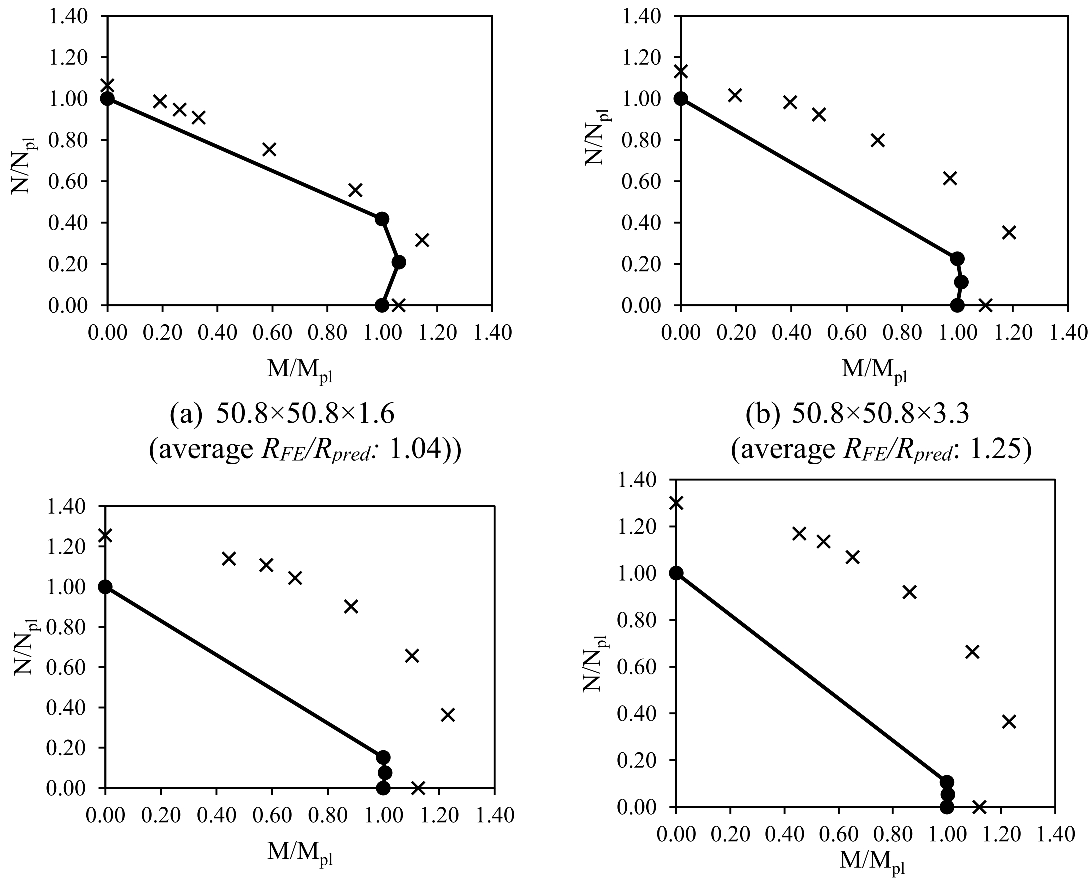

(a) 50.8×50.8×1.6 (average R_{FE}/R_{pred}: 1.04))

(b) 50.8×50.8×3.3 (average R_{FE}/R_{pred}: 1.25)

(c) 50.8×50.8×4.8 (average R_{FE}/R_{pred}: 1.47)

(d) 50.8×50.8×6.4 (average R_{FE}/R_{pred}: 1.51)

Fig. 15. Parametric study results of specimen 50.8 × 50.8 (aspect ratio 1).

4. Design recommendations

This section uses the obtained experimental and numerical performance data to assess the suitability of existing design guidelines for predicting the ultimate behaviour of CFAT cross-sections under combined compression and bending, with particular focus on European design guidelines. EC4 [31] provides guidance for steel–concrete composite members and EC9 [32] covers aluminium structural design, but there is no specific framework for aluminium–concrete composite columns. It is noteworthy that the recently updated version of EC9 [32] now includes provisions for I-section aluminium–concrete beams with shear connectors; however, there is still no direct guidance for concrete-filled aluminium tubular sections. Therefore, this study integrates and adapts relevant provisions from both Eurocodes 9 and 4 to evaluate their applicability in predicting combined moment–compression cross-sectional behaviour. Section 4.1 outlines the current guidelines of [31] and [32], while Section 4.2 presents the assessment based on experimental and numerical results.

4.1. Eurocode design provisions

For concrete-filled aluminium tubular cross-sections under combined axial compression and bending, a simplified M–N interaction curve adapted from the principles of EC4 and EC9 is employed, following the approach recommended in [31]. The suggested simplified M-N curve is constructed by four points, as shown in Fig. 12. The curve is defined by four characteristic points (A–D)

(1) Point A represents pure axial compression ($M = 0$)
(2) Point B corresponds to pure bending ($N = 0$)
(3) Point C combines the full plastic moment capacity with the axial resistance of the concrete infill, and
(4) Point D is defined by the maximum bending resistance associated with half of the plastic axial resistance.

Linear interpolation between these points is used to construct the interaction curve.

At point A, the cross-section is under pure compression, therefore $M_A = 0$ and the plastic resistance ($N_{pl,Rd}$) is determined according to Eq. 3. At Point B ($N_B = 0$), the cross-section is under pure bending and the plastic moment resistance ($M_{pl,Rd}$) is given by Eq. 4, where W_{pa} and W_{pc} are the plastic section moduli for the aluminium and concrete, respectively $W_{pa,n}$, $W_{pc,n}$ are the plastic section moduli for aluminium and concrete at the height of $2h_n$, respectively, where h_n is the depth of neutral axis. The moment at Point C is equal to $M_{pl,Rd}$ and N_C is the compression resistance provided by the concrete infill, as given in Eq. 5. Finally, Point D is defined by the maximum moment ($M_{\max,Rd}$) and half of $N_{pm,Rd}$ as described in Eq. 6

$$\text{Point } A: \ N_A = N_{pl} = A_a f_a + A_c f_c \text{ and } M_A = 0 \tag{3}$$

$$\text{Point } B: \ M_B = M_{pl} = (W_{pa} - W_{pa,n}) f_a + \frac{1}{2}(W_{pc} - W_{pc,n}) f_c \text{ and } N_B = 0 \tag{4}$$

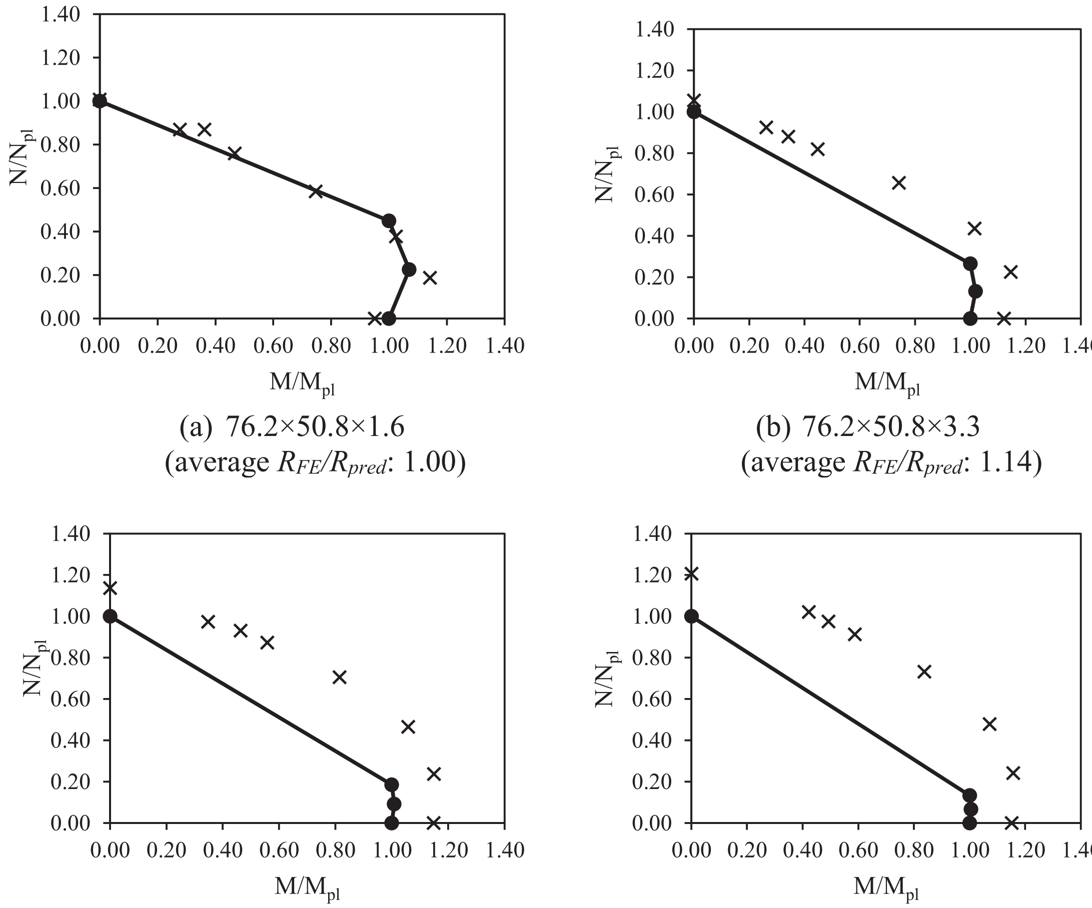

(a) 76.2×50.8×1.6 (average R_{FE}/R_{pred}: 1.00)

(b) 76.2×50.8×3.3 (average R_{FE}/R_{pred}: 1.14)

(c) 76.2×50.8×4.8 (average R_{FE}/R_{pred}: 1.26)

(d) 76.2×50.8×6.4 (average R_{FE}/R_{pred}: 1.33)

Fig. 16. Parametric study results of specimen 76.2 × 50.8 (aspect ratio:1.5) under major axis bending and compression.

$$\text{Point } C: \; M_C = M_B \text{ and } N_C = N_{pm,Rd} = A_c f_c \tag{5}$$

$$\text{Point } D: \; M_D = M_{\max,Rd} = W_{pa} f_a + \frac{1}{2} W_{pc} f_c \text{ and } N_D = \frac{1}{2} Npm_{,Rd} \tag{6}$$

4.2. Assessment based on test and FE data

For the assessment of the accuracy of design predictions, the ratio defined in Fig. 13 has been employed. According to this graph, the line from (0,0) to the intersection with the design interaction curve represents the predicted design capacity R_{pred} while the line from the origin (0,0) to the test/FE performance point is expressed by R_{Exp} *or* R_{FE}. The ratio of experimental or FEA results to the predicted capacity ($R_{\text{Exp,FE}}/R_{pred}$) can then be calculated. For ratio values exceeding unity, which lie outside the interaction curve, the design prediction is safe, with points extending beyond the curve indicating overly conservative estimates. Conversely, any points located inside the curve suggest unsafe design predictions.

By combining [31] and [32] design provisions, this section presents the normalised ultimate capacity of the composite CFAT cross-sections and their comparison with the Eurocode interaction curves. Firstly, the assessment is presented graphically including in the same graph the normalised test/FE data of a cross-section and the Eurocode design interaction curve corresponding to this cross-section. In all cases, the ultimate load was normalised by N_{pl} (see Eq. (3)) and the corresponding experimentally or numerically achieved moment was normalised by M_{pl} (see Eq. (4)). The points on the vertical axis correspond to the case of axial compression ($\psi = 1$), while the points on the horizontal axis correspond to the case of pure bending ($\psi = -1$). All the intermediate points correspond to the other ψ cases studied (0.65, 0.35, −0.65, −0.35, 0, 0.35, 0.50, 0.65).

Fig. 14 uses the normalised experimental data points presented in Section 2.4 to assess the Eurocode design predictions. In addition, the figure includes test data from the study by Gkantou et al. [26], which has studied the same CFAT cross-sections for the cases of axial compression and pure bending. Fig. 15-Fig. 19 present the results from the numerical parametric studies presented in Section 3.3. Each figure shows the behaviour of the same cross-section under different combinations of examined uniaxial bending and axial compression loadings. In particular,

Fig. 15 shows the results for SHS (50.8 × 50.8 mm) examined in four different thicknesses (a to d). Fig. 16 and Fig. 17 present the assessment for rectangular hollow sections with an aspect ratio of 1.5, under major and minor axis bending, respectively. Fig. 18 and Fig. 19 illustrate the results for rectangular hollow sections with an aspect ratio of 2, again for the cases of major and minor axis bending, respectively.

These figures indicate that overall, the design predictions offer a safe design margin. Both the experimental and finite element results follow the interaction curve, with a safety margin that tends to be conservative for sections with higher cross-sectional thickness. This also reflects the ability of sections with higher thickness to develop their full plastic moment capacity. Comparable findings have been reported for bare stub column sections under eccentric compression [39]. While most FE cases remain within a reasonably safe margin, the higher values – particularly for 50.8 × 50.8 × 6.4 – highlight the need for further scrutiny in design

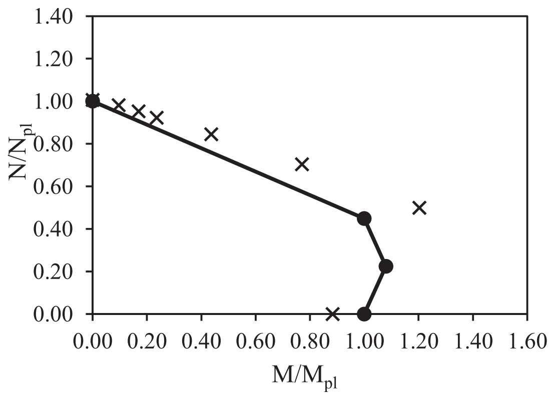

(a) 50.8×76.2×1.6
(average R_{FE}/R_{pred}: 1.04)

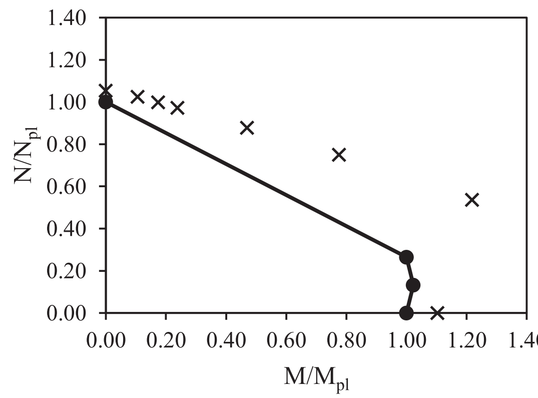

(b) 50.8×76.2×3.3
(average R_{FE}/R_{pred}: 1.19)

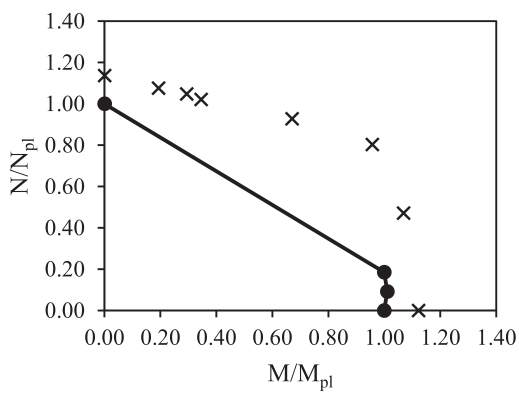

(c) 50.8×76.2×4.8
(average R_{FE}/R_{pred}: 1.31)

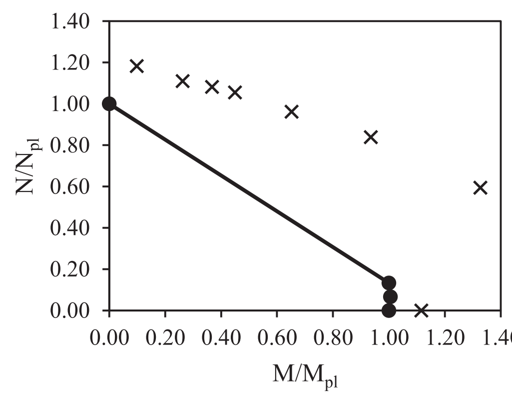

(d) 50.8×76.2×6.4
(average R_{FE}/R_{pred}: 1.43)

Fig. 17. Parametric study results of specimen 76.2 × 50.8 (aspect ratio:1.5) under minor axis bending and compression.

to avoid overutilisation in specific scenarios. It is noteworthy that, according to [31], only sections with a width-to-thickness ratio $h/t \leq 52 (235/f_y)^{0.5}$ are recommended for use in concrete-filled steel members, effectively excluding Class 4 sections. This can be translated for aluminium structures as a limit of $h/t \leq 52(250/f_{0.2})^{0.5}$, substituting the $235/f_y$ with $250/f_{0.2}$ based on [32]. From the parametric study presented herein, only the FE results shown in Fig. 18(a) and Fig. 19(a) do not comply with this limit ($h/t = 101.6/1.6 = 64 > 52(250/271.20)^{0.5} = 50$). Nevertheless, they have been included in the assessment using the same design formulae as the rest. Their overall performance for these two sections was reasonable, closely following the Eurocode interaction curve. However, the resulting design values were slightly unconservative, with R_{FE}/R_{pred} ratios of 0.96 and 0.95, indicating the need to consider adopting a similar slenderness limit for CFAT columns. It is also noted that for thinner aluminium sections more linear axial load–moment interaction response is observed.

Further to the graphical presentation, a quantitative assessment is presented in Table 6 and Table 7, showing the average $R_{\mathrm{Exp,FE}}/R_{pred}$ values for the examined parameters. Table 6 presents all the corresponding $R_{\mathrm{Exp,FE}}/R_{pred}$ ratios of examined sections, while Table 7 shows the average values calculated to evaluate the influence of the key parameters considered. The FE results span a broad range of sizes and thicknesses, with $R_{\mathrm{Exp,FE}}/R_{pred}$ values ranging from 0.95 to 1.51. The FE predictions generally follow similar trends to the experimental data, with thicker sections resulting higher $R_{\mathrm{Exp,FE}}/R_{pred}$ values. The sections 50.8 × 50.8 × 3.3 and 50.8 × 50.8 × 4.7 mm, which were studied both experimentally and numerically, yielded very similar $R_{\mathrm{Exp,FE}}/R_{pred}$ values: 1.26 and 1.39 from the tests, and 1.25 and 1.47 from the numerical analyses. Overall, the mean R value of 1.19 with a coefficient of variation of 0.16 indicates that the combined EC4–EC9 framework provides generally conservative and reasonably consistent predictions for SHS CFAT stub columns under eccentric loading, demonstrating promising performance as a design-oriented assessment approach within the scope of the present study.

The average R_{FE}/R_{pred} values for various examined eccentricities have a peak observed around $\psi = -0.35$ with average R_{FE}/R_{pred} values of 1.25. For sections subjected to ψ values from 1 to 0, the R increases gradually from 1.09 to 1.24, indicating more conservative outcomes as the load transitions from pure compression to combined bending and compression. For ψ equal to −0.35, the highest ratio values are observed, reflecting the most conservative predictions, suggesting that the structural capacity is underutilised under these load combinations. This behaviour indicates that the adapted interaction approach remains on the safe side across the full range of axial load–moment combinations considered, with no evidence of systematic unconservative predictions.

With respect to the effect of the aluminium tube thickness, R_{FE}/R_{pred} increases from 1.00 to 1.32 as thickness increases. This trend also reflects the influence of lower slenderness (h/t), which reduces susceptibility to local buckling and results in more conservative design predictions. The thickness-dependent increase in conservatism suggests that, while the Eurocode-based approach provides reasonable predictions within the investigated range, further validation and refinement

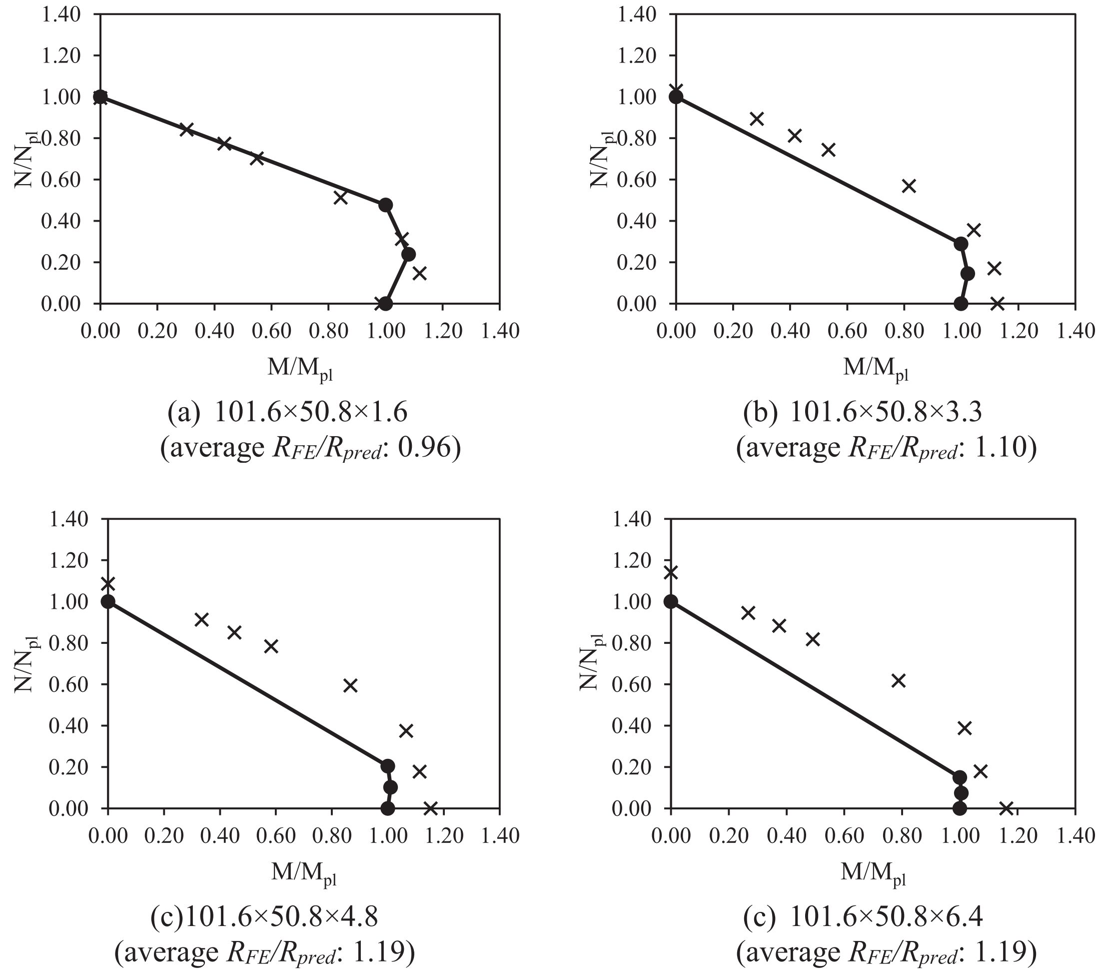

Fig. 18. Parametric study results for 101.6 × 50.8 mm specimens (aspect ratio 2.0) under major axis bending and compression.

are required to better capture sectional slenderness effects.

In terms of the cross-sectional aspect ratio and applied bending axis, sections with an aspect ratio of 1 exhibit the highest average ratio value of 1.32, indicating the most conservative estimations. Similar trends are observed for bending around the major and minor axes sections. Based on the present dataset, no new interaction formulation appears necessary; however, the results highlight the importance of sectional slenderness and thickness effects in future calibration of CFAT-specific design provisions. The adapted EC4–EC9 framework shows good agreement with the experimental and numerical results and provides a preliminary assessment approach for SHS CFAT stub columns within the investigated range of parameters, while the sensitivity to sectional slenderness and thickness highlights parameters that warrant further calibration in future design development.

Finally, Table 8 summarises collated literature data on concrete-filled aluminium tubular cross-sections in order to assess the proposed framework. The collated data focus on square and rectangular concrete-filled aluminium stub columns and beams. Studies on long columns and circular sections were excluded to ensure consistency with the investigated specimens. The reviewed studies considered aluminium grades 6061-T6, 6082-T6, and 5083 with concrete strengths ranging from C20 to C50, comprising a total of 63 tests. The evaluated mean experimental-to-predicted resistance ratios (R_{Exp}/R_{pred}) range from 0.98 to 1.17, with an overall average of 1.04, indicating good agreement between experimental and predicted capacities. The literature review also highlights a research gap, as no previous studies were identified on SHS concrete-filled aluminium members subjected to eccentric compression or combined loading behaviour, demonstrating the contribution and novelty of the present study.

5. Conclusions

This paper presents an experimental and numerical study to investigate the cross-sectional performance of concrete-filled aluminium tubes under eccentric axial compression.

- A total of eight columns with two different cross-sections were tested under nominal eccentricities of 0, 5, 10, and 15 mm. Both specimen groups exhibited significant plastic deformation; however, no major surface spalling or visible concrete cracking was observed. Local buckling near the specimen ends was also noted, mainly under concentric loading.
- Increasing eccentricity progressively shifts the response from compression-dominated to bending–compression interaction behaviour, reducing the confinement effect provided by the aluminium tube to the internal concrete. In addition, the tube thickness and section slenderness are dominant parameters governing confinement efficiency and ultimate capacity.
- A finite element model was developed and validated against a total 27 test data. Comparison of ultimate loads showed excellent agreement, with an average $N_{u,FE}/N_{u,Test}$ ratio of 0.99 with a coefficient of variation of 0.04, confirming the robustness of the adopted modelling strategy for interaction analysis.
- A numerical parametric study comprising 160 cases was conducted, enabling the generation of additional performance data and the evaluation of the influence of key parameters.

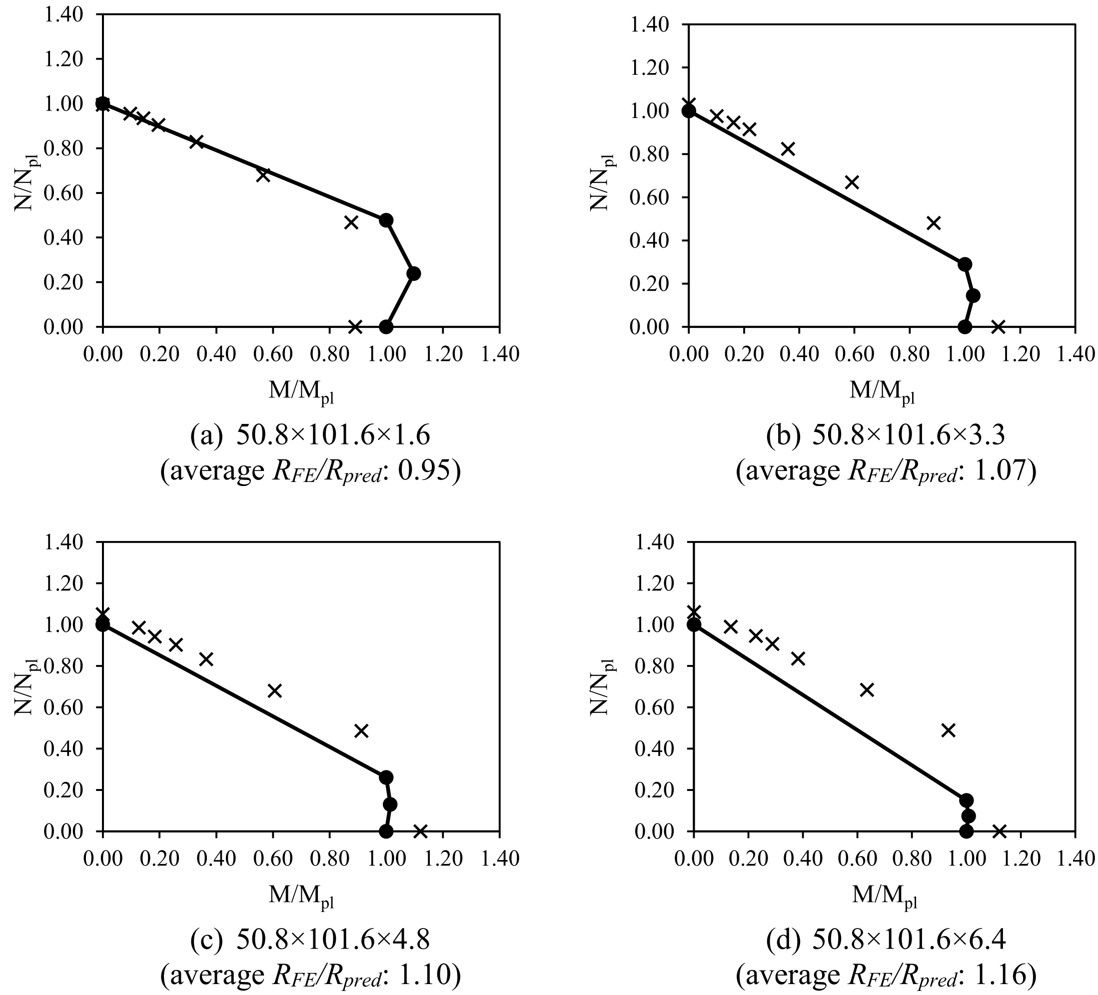

Fig. 19. Parametric study results for 50.8 × 101.6 mm specimens (aspect ratio 2.0) under minor axis bending and compression.

Table 6
Quantitative assessment: $R_{Exp,FE}/R_{pred}$ ratios based on Eurocode interaction curves.

	Experimental results									
	Corresponding Figures	**e0**	e5	**e10**	**e15**	**ψ= −1**		**ψ= 1**		**Average (specimen)**
50.8 × 50.8 × 3.3	Fig. 14(a)	1.16	1.21	1.28	1.25	1.34		1.31		1.26
50.8 × 50.8 × 4.8	Fig. 14(b)	1.35	1.40	1.55	1.48	1.30		1.24		1.39
	Finite Element results									
cross-section	**Corresponding Figures**	**1**	**0.65**	**0.50**	**0.35**	**0**	**−0.35**	**−0.65**	**−1**	**Average (specimen)**
50.8 × 50.8 × 1.6	Fig. 15(a)	1.02	1.05	1.05	1.06	1.05	1.03	1.04	1.00	1.04
50.8 × 50.8 × 3.3	Fig. 15(b)	1.13	1.17	1.29	1.31	1.35	1.37	1.27	1.10	1.25
50.8 × 50.8 × 4.8	Fig. 15(c)	1.25	1.52	1.60	1.62	1.65	1.59	1.41	1.13	1.47
50.8 × 50.8 × 6.4	Fig. 15(d)	1.30	1.58	1.62	1.65	1.69	1.64	1.47	1.12	1.51
76.2 × 50.8 × 1.6	Fig. 16(a)	1.01	1.01	1.05	0.99	0.95	0.98	1.07	0.95	1.00
76.2 × 50.8 × 3.3	Fig. 16(b)	1.05	1.12	1.13	1.15	1.20	1.18	1.14	1.12	1.14
76.2 × 50.8 × 4.8	Fig. 16(c)	1.14	1.26	1.31	1.33	1.37	1.33	1.18	1.15	1.26
76.2 × 50.8 × 6.4	Fig. 16(d)	1.21	1.39	1.40	1.42	1.46	1.41	1.24	1.15	1.33
50.8 × 76.2 × 1.6	Fig. 17(a)	1.01	1.03	1.04	1.04	1.06	1.08	1.17	0.88	1.04
50.8 × 76.2 × 3.3	Fig. 17(b)	1.05	1.10	1.13	1.15	1.22	1.32	1.43	1.10	1.19
50.8 × 76.2 × 4.8	Fig. 17(c)	1.14	1.23	1.29	1.30	1.47	1.58	1.34	1.12	1.31
50.8 × 76.2 × 6.4	Fig. 17(d)	1.19	1.34	1.40	1.45	1.53	1.65	1.75	1.12	1.43
101.6 × 50.8 × 1.6	Fig. 18(a)	0.99	0.97	0.96	0.94	0.85	0.94	1.05	0.99	0.96
101.6 × 50.8 × 3.3	Fig. 18(b)	1.03	1.09	1.11	1.12	1.14	1.09	1.09	1.13	1.10
101.6 × 50.8 × 4.8	Fig. 18(c)	1.09	1.18	1.21	1.25	1.28	1.22	1.11	1.15	1.19
101.6 × 50.8 × 6.4	Fig. 18(d)	1.14	1.17	1.20	1.24	1.29	1.25	1.09	1.16	1.19
50.8 × 101.6 × 1.6	Fig. 19(a)	0.99	1.00	1.00	0.99	0.97	0.92	0.86	0.89	0.95
50.8 × 101.6 × 3.3	Fig. 19(b)	1.03	1.05	1.06	1.07	1.08	1.08	1.11	1.12	1.07
50.8 × 101.6 × 4.8	Fig. 19(c)	1.05	1.08	1.08	1.09	1.10	1.12	1.15	1.12	1.10
50.8 × 101.6 × 6.4	Fig. 19(d)	1.06	1.11	1.14	1.15	1.16	1.22	1.28	1.12	1.16
Mean (All)										1.19
COV (All)										0.16

Table 7
Average values of R_{FE}/R_{pred}, examining different parameters.

(a) average R_{FE}/R_{pred} based on ψ ratio

ψ ratio	**1**	**0.65**	**0.5**	**0.35**	**0**	**−0.35**	**−0.65**	**−1**
R_{FE}/R_{pred}	1.09	1.17	1.20	1.22	1.24	1.25	1.21	1.08

(b) average R_{FE}/R_{pred} based on thicknesses

t (mm)	**1.6**	**3.3**	**4.8**	**6.4**
R_{FE}/R_{pred}	1.00	1.15	1.26	1.32

(c) average R_{FE}/R_{pred} based on bending axis

h/b – Bending axis	**h/b= 1**	**Major Axis**	**Minor Axis**
R_{FE}/R_{pred}	1.32	1.18	1.16

Table 8
Summary of collated literature data for square and rectangular concrete-filled aluminium stub columns and beams.

	Aluminium grade	concrete grade	cross-section type	Loading type	No of tests	Mean R_{Exp}/R_{pred}
Deng at al. [29]	6061-T6	C20, C30, C40	SHS	pure compression	9	1.00
Feng et al. [18]	5083	C30, C50	SHS & RHS	pure bending	20	0.98
Bin et al. [15]	6082-T6	C20	SHS & RHS	pure bending	10	1.17
Gkantou et al. [26]	6082-T6	C30	SHS	pure compression	16	1.00
Gkantou et al. [26]	6082-T6	C30	SHS	pure bending	8	1.12
				All	63	1.04

- Increasing the aluminium tube thickness leads to higher conservatism, with R_{FE}/R_{pred} values rising from 1.00 (for 1.6 mm thickness) to 1.32 (for 6.4 mm thickness), showing the effect of h/t slenderness parameter. The most conservative predictions occur around $\psi = -0.35$ with average R_{FE}/R_{pred} values of 1.25. When considering all applied eccentricities, both major and minor axis bending demonstrated relatively conservative estimates.
- Overall, the combined application of Eurocode 9 and Eurocode 4 provided satisfactory predictions when assessed against both experimental and numerical results, with an average $R_{\text{Exp,FE}}/R_{pred}$ ratio of 1.19.
- While most FE results fall within an acceptable safety margin, the higher R_{FE}/R_{pred} values associated with thicker sections indicate the need for further scrutiny to avoid over-conservatism in design. In contrast, R_{FE}/R_{pred} values lower than unity for sections with higher h/t suggest that the introduction of a slenderness limit for CFAT columns-similar to that adopted for CFST columns-may be warranted. These observations highlight sectional slenderness as a key parameter requiring further calibration.
- The results confirm that the adapted EC4–EC9 interaction framework provides a reasonable design-oriented assessment for SHS CFAT stub columns under eccentric loading within the investigated range of parameters. The observed thickness- and slenderness-dependent behaviour highlights the need for further validation and provides clear directions for future refinement of CFAT-specific provisions.

The key contribution of this work is the establishment of a validated CFAT-specific axial load–moment interaction framework for aluminium–concrete composite cross-sections, supported by new experimental evidence on 6082-T6 SHS CFAT cross-sections under combined axial compression and bending. The proposed approach enables a design-oriented assessment of CFAT cross-sections within the investigated range of parameters and supports the future development of refined design guidance for CFAT members.

Future research could extend the present work to address aspects not covered herein. An important next step is the extension of the proposed framework to account for global buckling behaviour in slender CFAT columns, enabling assessment beyond cross-sectional response. Direct comparisons between CFAT and conventional CFST members on an equal-weight basis, particularly with respect to load-bearing capacity and structural efficiency, would also provide valuable insight and are recommended for future study. Further investigations could examine the influence of higher-strength, sustainable, and durability-enhanced concrete grades on CFAT behaviour, together with the long-term durability and corrosion performance of concrete-filled aluminium alloy tubular members. Moreover, addressing behaviour under elevated temperatures, post-fire conditions, and dynamic or cyclic loading would further contribute to a more comprehensive understanding of CFAT members and support the continued development of robust and reliable design guidance.

CRediT authorship contribution statement

Shafayat Bin Ali: Writing – original draft, Investigation. **Michaela Gkantou:** Writing – review & editing, Writing – original draft, Investigation, Conceptualization. **Yao Sun:** Writing – review & editing. **Nikolaos I. Tziavos:** Writing – original draft, Investigation.

Declaration of Competing Interest

The authors declare that they have no known competing financial interests or personal relationships that could have appeared to influence the work reported in this paper.

Acknowledgements

The authors would like to thank the Faculty of Health, Innovation, Technology and Science of Liverpool John Moores University for their financial support. They would also like acknowledge the support received from Mr. Richard Clarke, technician at the School of Engineering and Built Environment, Liverpool John Moores University, for his assistance with the experimental work.

References

[1] Roeder CW, Lehman DE, Bishop E. Strength and stiffness of circular concrete-filled tubes. J Struct Eng Dec. 2010;136(12):1545–53. https://doi.org/10.1061/(ASCE)ST.1943-541X.0000263.
[2] Yang H, Lam D, Gardner L. Testing and analysis of concrete-filled elliptical hollow sections. Eng Struct Dec. 2008;30(12):3771–81. https://doi.org/10.1016/j.engstruct.2008.07.004.
[3] Tziavos NI, Gkantou M, Theofanous M, Dirar S, Baniotopoulos C. Behaviour of grout-filled double-skin tubular steel stub-columns: numerical modelling and design considerations. Structures Oct. 2020;27:1623–36. https://doi.org/10.1016/j.istruc.2020.07.021.

[4] Lai MH, Song W, Ou XL, Chen MT, Wang Q, Ho JCM. A path dependent stress-strain model for concrete-filled-steel-tube column. Eng Struct May 2020;211:110312. https://doi.org/10.1016/j.engstruct.2020.110312.
[5] Ren FM, et al. GFRP – sea water sea sand coral concrete – high strength steel composite column: concept and axial compressive behavior. Thin-Walled Struct Oct. 2025;215:113487. https://doi.org/10.1016/j.tws.2025.113487.
[6] Young B, Ellobody E. Experimental investigation of concrete-filled cold-formed high strength stainless steel tube columns. J Constr Steel Res May 2006;62(5):484–92. https://doi.org/10.1016/j.jcsr.2005.08.004.
[7] Zhao XL, Packer JA. Tests and design of concrete-filled elliptical hollow section stub columns. Thin-Walled Struct Jun. 2009;47(6–7):617–28. https://doi.org/10.1016/j.tws.2008.11.004.
[8] Lam D, Gardner L. Structural design of stainless steel concrete filled columns. J Constr Steel Res Nov. 2008;64(11):1275–82. https://doi.org/10.1016/j.jcsr.2008.04.012.
[9] Guo L, Zhang S, Kim W-J, Ranzi G. Behavior of square hollow steel tubes and steel tubes filled with concrete. Thin-Walled Struct Dec. 2007;45(12):961–73. https://doi.org/10.1016/j.tws.2007.07.009.
[10] Feng P, Cheng S, Bai Y, Ye L. Mechanical behavior of concrete-filled square steel tube with FRP-confined concrete core subjected to axial compression. Compos Struct May 2015;123:312–24. https://doi.org/10.1016/j.compstruct.2014.12.053.
[11] Georgantzia E, Gkantou M, Kamaris GS. Aluminium alloys as structural material: A review of research. Eng Struct Jan. 2021;227:111372. https://doi.org/10.1016/j.engstruct.2020.111372.
[12] Sun Y. The use of aluminum alloys in structures: Review and outlook. Structures Nov. 2023;57:105290. https://doi.org/10.1016/j.istruc.2023.105290.
[13] Zeng X, Ning C, Zeng W, Xu B. Numerical and experimental studies on bending behavior of circular aluminium-concrete-steel double skin tubular cross-sections and bending capacity design approach. J Build Eng Aug. 2024;91:109524. https://doi.org/10.1016/j.jobe.2024.109524.
[14] Ali SBin, Kamaris GS, Gkantou M, Huang Y. Comparative Study of Life-Cycle Environmental and Cost Performance of Aluminium Alloy–Concrete Composite Columns. Sustainability Oct. 2024;16(21):9252. https://doi.org/10.3390/su16219252.
[15] Ali SBin, Kamaris GS, Gkantou M, Kansara KD. Concrete-filled and bare 6082-T6 aluminium alloy tubes under in-plane bending: Experiments, finite element analysis and design recommendations. Thin-Walled Struct Mar. 2022;172:108907. https://doi.org/10.1016/j.tws.2022.108907.
[16] Zhou F, Young B. Tests of concrete-filled aluminum stub columns. Thin-Walled Struct Jun. 2008;46(6):573–83. https://doi.org/10.1016/j.tws.2008.01.003.
[17] Zhou F, Young B. Concrete-filled aluminum circular hollow section column tests. Thin-Walled Struct Nov. 2009;47(11):1272–80. https://doi.org/10.1016/j.tws.2009.03.014.
[18] Feng R, Chen Y, Gong W. Flexural behaviour of concrete-filled aluminium alloy thin-walled SHS and RHS tubes. Eng Struct 2017;137:33–49. https://doi.org/10.1016/j.engstruct.2017.01.036.
[19] Chen X, Huang H, Hassam M, Guo L. Eccentric compressive behavior of circular concrete-filled aluminum alloy tubular columns. Structures Dec. 2025;82:110412. https://doi.org/10.1016/j.istruc.2025.110412.
[20] Georgantzia E, Bin Ali S, Gkantou M, Kamaris GS, Kansara KD, Atherton W. Flexural buckling performance of concrete-filled aluminium alloy tubular columns. Eng Struct Sep. 2021;242:112546. https://doi.org/10.1016/j.engstruct.2021.112546.
[21] Rong B, Zhang S, Zhang Y, Liu H, Li Z. Study on the ultimate bearing capacity of 7A04-T6 CFAT columns under eccentric compression. J Build Eng Apr. 2022;46:103654. https://doi.org/10.1016/j.jobe.2021.103654.
[22] Rong B, Zhai X, Li Z, Cheng H, Dong A, Zhang R. Study on axial compression behavior of 7A04-T6 concrete-filled aluminum tubular columns. J Build Eng Oct. 2023;76:107118. https://doi.org/10.1016/j.jobe.2023.107118.
[23] Mi Q, Shu Q, Wang F, Liu P, Zhu M, Wang W. Experimental study on eccentric compressive behaviors of 6061-T6 aluminum tubular long columns filled with concrete. Eng Struct Jan. 2024;299:117040. https://doi.org/10.1016/j.engstruct.2023.117040.
[24] Guo J, Wang Y, Deng Z, Chang P. Research on the axial compression performance of coral concrete-filled aluminum alloy tube columns. Case Stud Constr Mater Jul. 2024;20:e02952. https://doi.org/10.1016/j.cscm.2024.e02952.
[25] Jiang J, et al. Mechanical behavior of coral concrete-filled aluminum alloy square tube columns subjected to eccentric loading. Structures Jun. 2025;76:108907. https://doi.org/10.1016/j.istruc.2025.108907.
[26] Gkantou M, Georgantzia E, Kadhim A, Kamaris GS, Sadique M. Geopolymer concrete-filled aluminium alloy tubular cross-sections. Structures May 2023;51:528–43. https://doi.org/10.1016/j.istruc.2023.02.117.
[27] He Z, Deng Z, Hu S, Liu B. Axial compression performance of coral concrete-filled aluminum alloy tube (CCFAT) circular short columns. Eng Struct Mar. 2024;303:117552. https://doi.org/10.1016/j.engstruct.2024.117552.
[28] He Z, Deng Z, Hu S, Jiang J, Liu B. Eccentric compression performance of coral concrete-filled aluminum alloy tube (CCFAT) circular short columns. Structures Nov. 2024;69:107314. https://doi.org/10.1016/j.istruc.2024.107314.
[29] Deng Z, Guo J, Yu J, Liu B. Axial compression performance of coral concrete-filled aluminium tube (CCFAT) square stub columns. Case Stud Constr Mater Dec. 2021;15:e00697. https://doi.org/10.1016/j.cscm.2021.e00697.
[30] You X, et al. A review of research on aluminum alloy materials in structural engineering. Dev Built Environ Mar. 2024;17:100319. https://doi.org/10.1016/j.dibe.2023.100319.
[31] EN 1994-1-1,. European Committee for Standardisation; 2005.
[32] EN 1999-1-1. Eurocode 9: Design of aluminium structures — Part 1-1: General structural rules. Brussels: CEN.," CEN. European Committee for Standardisation; 2023.
[33] Bin Ali S, Kamaris GS, Gkantou M. Flexural buckling behaviour of concrete-filled double skin aluminium alloy columns. Eng Struct Jan. 2023;275:115316. https://doi.org/10.1016/j.engstruct.2022.115316.
[34] BS EN ISO 6892-1, "Metallic materials. Tensile testing. Method of test at room temperature," 2019.
[35] Ramberg W, Osgood WR. Descr Stress-strain curves three Parameters 1943.
[36] Hill HN. Determ Stress-strain Relat " Offset" yield Strength Values 1944.
[37] Bin Ali S, Kamaris GS, Gkantou M. Flexural behaviour of concrete-filled double skin aluminium alloy tubes. Eng Struct Dec. 2022;272:114972. https://doi.org/10.1016/j.engstruct.2022.114972.
[38] BS EN 12390-3, "Testing hardened concrete. Compressive strength of test specimens," 2019.
[39] Gkantou M, Theofanous M, Wang J, Baniotopoulos C, Gardner L. Behaviour and design of high-strength steel cross-sections under combined loading. Proc Inst Civil Eng Struct Build 2017;170(11). https://doi.org/10.1680/jstbu.16.00114.
[40] S.I. Karlsson Hibbitt, "ABAQUS/Standard User's Manual Volumes I-III and ABAQUS CAE Manual," 2016.
[41] Tao Z, Wang Z-B, Yu Q. Finite element modelling of concrete-filled steel stub columns under axial compression. J Constr Steel Res Oct. 2013;89:121–31. https://doi.org/10.1016/j.jcsr.2013.07.001.
[42] Papanikolaou VK, Kappos AJ. Confinement-sensitive plasticity constitutive model for concrete in triaxial compression. Int J Solids Struct Oct. 2007;44(21):7021–48. https://doi.org/10.1016/j.ijsolstr.2007.03.022.
[43] Yu T, Teng JG, Wong YL, Dong SL. Finite element modeling of confined concrete-I: drucker–Prager type plasticity model. Eng Struct Mar. 2010;32(3):665–79. https://doi.org/10.1016/j.engstruct.2009.11.014.
[44] D. Hordijk, "Local approach to fatigue of concrete,": Delft University of Technology, 1991.
[45] FIP, "Ceb-Fip Model Code 1990," 1990.
[46] Bažant ZP, Becq-Giraudon E. Statistical prediction of fracture parameters of concrete and implications for choice of testing standard. Cem Concr Res Apr. 2002;32(4):529–56. https://doi.org/10.1016/S0008-8846(01)00723-2.
[47] Mazzolani F. Alum Alloy Struct 1994.
[48] Wang J-X, Liu F, Gao S. Axial compressive behavior of aluminum alloy thin-walled tube confined concrete. Constr Build Mater Mar. 2025;467:140350. https://doi.org/10.1016/j.conbuildmat.2025.140350.